Muon Identification with Kalman Filter at KEK B-Factory

Hideki Miyake

Osaka University

April 19, 2000

Acknowledgments

Abstract

The KEK B-factory is a facility to study $\mathbf{CP}$ violation in the B meson system with producing a large number of B mesons. Identification of muons at the KEK B-factory is important as the most promising decay mode of B mesons is $B \to J/\psi K_S$ where J/ψ further decays into $\mu^+\mu^-$ and e^+e^-. In order to identify muons efficiently, we developed muon identification software adopting Kalman filter algorithm. By evaluating its performance with Monte Carlo simulation and real data taken at the KEK B-factory in 1999, it is proven that the Kalman filter is an effective tool to identify muons. In the end, we demonstrated the reconstruction of inclusive B decays into J/ψ where J/ψ's were tagged with dimuons. From the signal yield of (136 ± 13) events collected with an integrated luminosity of 239 pb^{-1}, the branching fraction was estimated to be $\mathbf{Br}(B \to J/\psi \mathrm{X}) = 0.83 \pm 0.08(\%)$, where the error is statistical only.

Contents

List of Figures

List of Tables

Chapter 1

Introduction

One of the hot topics of the elementary particle physics (high energy physics) nowadays is **CP** violation which was first observed in the decay of neutral K mesons by V.L.Fitch and J.W.Cronin et al in 1964 [1]. This broken symmetry under Charge and Parity conjugation means that interactions among particles are different from that of antiparticles. Thus it is one of necessary conditions to explain why our universe is dominated by matter but not antimatter [2].

As well known, the Standard Model (SM) [3] in the elementary particle physics has been supported by many experimental results. In 1973, Kobayashi and Maskawa (KM) published one quite interesting paper, today known as the KM model, which explained the origin of the **CP** violation within the framework of the SM, and predicted that there would be at least six quark flavors, twice the number of quark flavors known at that time. This was later proven by the discoveries of c, b and t quarks [4]. Nevertheless the origin of the **CP** violation itself is not yet confirmed.

In 1980, Sanda and Carter pointed out the possibility that large **CP** asymmetry would be seen in the decays of neutral B mesons according to the KM model which is now an essential part of the SM [5]. Several experimental projects to observe such **CP** violation producing a large number of B mesons, which are generally called "B-Factories", were planned since then.

The KEK B-factory [6], which consists of the KEKB acceralator and the BELLE detector, is one of them. The features of the KEK B-factory are very high luminosity of 10^{34}cm^{-2}s^{-1} , asymmetric collisions at a $\beta\gamma$ of 0.425 (8.0GeV/c electrons on 3.5 GeV/c positrons), optimized detector components with a precise vertex reconstruction capability and efficient particle

identification (PID) system.

Among various roles of the BELLE detector, identification of muons at the KEK B-factory plays an essential role as the most promising decay mode of the B meson is $B \to J/\psi K_S$ where J/ψ further decays into $\mu^+\mu^-$ and e^+e^-.

In this thesis, we developed muon reconstruction software with a new idea based on the "Kalman filter" algorithm[10] and studied its performance with real data. In Chapter 2, the physics motivation of the B-factory is explained with a special emphasis on muon identification. The experimental apparatus of the KEK B-factory is explained in Chapter 3, followed by the characteristics of muons inside the BELLE detector in Chapter 4. After describing the Kalman filter algorithm and its application to the BELLE muon identification system in Chapter 5, the performance of the muon identification software is given in Chapter 6. We conclude this study in Chapter 7.

Chapter 2

Motivation for Muon Identification at KEK B-Factory

2.1   CP violation in B decays

At the KEK B-factory, electrons and positrons collide to produce the $\Upsilon(4S)$ mesons which decay into pairs of B mesons. The main purpose of the KEK B-factory is to observe time-dependent **CP** asymmetry expected to arise when one of two neutral B mesons decays into a **CP** eigenstate (denoted by $f_{\mathbf{CP}}$) and the other into a final state (denoted by $f_{\mathbf{TAG}}$) that comes from a specific b-flavor (called a flavor-specific decay). At the time of the flavor-specific decay, the other B has a definite b-flavor, i.e. it is either B^0 or $\bar{B}^0$. As time passes, it becomes a mixture of B^0 and $\bar{B}^0$ due to the B^0-$\bar{B}^0$ mixing (B^0 becomes $B^0(t)$ and $\bar{B}^0$ to $\bar{B}^0(t)$). The time dependent decay-rate asymmetry is defined as

$$a_{f_{\mathbf{CP}}}(\Delta t) \equiv \frac{\Gamma(\bar{B}^0(\Delta t) \to f_{\mathbf{CP}}) - \Gamma(B^0(\Delta t) \to f_{\mathbf{CP}})}{\Gamma(\bar{B}^0(\Delta t) \to f_{\mathbf{CP}}) + \Gamma(B^0(\Delta t) \to f_{\mathbf{CP}})}, \qquad (2.1)$$

where Δt is the decay time difference between $B \to f_{\mathbf{CP}}$ and $B \to f_{\mathbf{TAG}}$. As $\bar{B}^0(t)$ is the **CP** conjugate of $B^0(t)$, a non-zero value of $a_{f_{\mathbf{CP}}}(\Delta t)$ means the **CP** violation.

The most promising final state for $f_{\mathbf{CP}}$ is $J/\psi K_S$. The Feynman diagram is shown in Figure 2.1. According to the SM, the asymmetry in this case is

$$a_{f_{\mathbf{CP}}}(\Delta t) = \sin 2\phi_1 \sin(\Delta M \Delta t), \qquad (2.2)$$
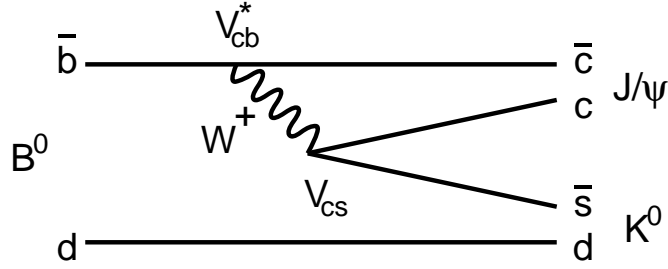
Figure 2.1: *Feynman diagram of $B^0 \rightarrow J/\psi K_S$.*

where ϕ_1 is an angle of the unitarity triangle and ΔM is the mass difference between two mass-eigenstates. The derivation of this equation as well as a theoretical framework of **CP** violation is given in Appendix A.

Among many decay modes of J/ψ , $J/\psi \rightarrow \mu^+\mu^-$ (as well as e^+e^-) has the largest branching ratio ($\sim 6\%$). In this case, expected background events are also exceedingly small. Therefore, it is important to identify these muons with a high efficiency as the precision of the $\sin 2\phi_1$ measurement will be dominated by the statistical error. Figure 2.2 shows the expected momentum distribution of muons in $B \rightarrow J/\psi (\rightarrow \mu\mu) K_S$ decay. As shown
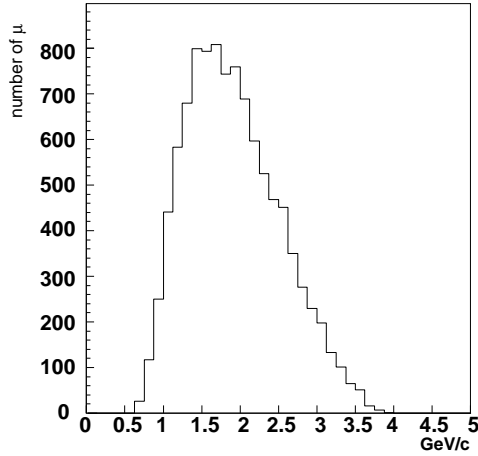
Figure 2.2: *Muon momentum ddistribution in $J/\psi (\rightarrow \mu\mu) k_S$ decay in the event generator (the vertical scale is arbitrary).*

4

in the figure, the momentum range is from 0.65 GeV/c to 3.9 GeV/c. As for the flavor specific decays, we do not have to reconstruct the B mesons exclusively, but it is enough to tag the flavor of the parent B meson. There are several ways of such "flavor tagging". One of them is to tag a high-momentum muon in semi-leptonic decays such as $B \to D\mu\nu$, $B \to D^*\mu\nu$, $B \to D^{**}\mu\nu$ etc. Figure 2.3 shows the momentum spectrum of such muons.
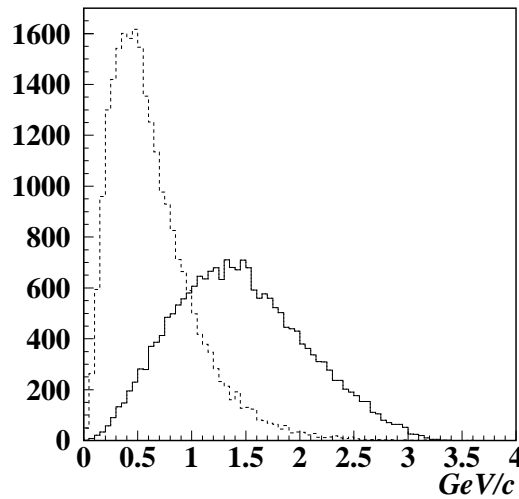
Figure 2.3: *Muon momentum distribution in generic B decays in the event generator.*
the solid line is for muons from b and the dashed line is for muons from c.

Also shown in the same figure are muons from charmed hadrons populated in the lower momentum region that can be easily distinguished.

2.2   Other Muons

Besides the observation of **CP** violation, it is also important at the KEK B-factory to measure the magnitudes of elements of the CKM matrix. The size of V_{cb} can be determined from both inclusive and exclusive semi-leptonic B decays with the $b \to c$ transition. Measurements of $|V_{ub}|$ are also impor-

5

tant but more challenging as the expected size is much smaller than $|V_{cb}|$. Measurements of muons (and electrons) above the kinematical limit of the $b \to c$ transition in inclusive semi-leptonic B decays provides a current experimental evidence for non-zero value of $|V_{ub}|$ [7, 8]. Another possibility is a measurement of exclusive semileptonic decays $\overline{B} \to X \ell \overline{\nu}$ where $X = \pi, \rho$, and ω and $l = \mu$ and e. Thoretical calculations for these modes are expected to be less uncertain than those for the inclusive modes, although the it must rely on form factors measured experimentally.

Muons are also important in searching for rare B decays such as $B \to \mu\mu$ and $K^*\mu\mu$. Lepton flavor-violating processes such as $B \to e\mu$ and $\mu\tau$ also require muon identification. Physics in τ lepton decays in the $e^+e^- \to \tau^+\tau^-$ process is often studied by tagging muons from the $\tau \to \mu\nu\nu$ decay.

Other processes such as $ee \to \mu\mu$, $ee \to \mu\mu\gamma$, and the 2 photon process $\gamma\gamma \to \mu\mu$ are quite useful to study the performance of muon identification with real data, as they cover a wide range of momentum region.

Chapter 3

Experimental Apparatus at KEK B-Factory

3.1 Overview

A B-factory is an experimental facility to observe **CP** violation with producing a large amount of B mesons. The KEK B-factory is one of them, at KEK (High Energy Accelerator Research organization), Japan. It consists of the KEKB accelerator and the BELLE detector. The KEKB accelerator is an electron-positron synchrotron collider characterised by 2 rings, high luminosity and asymmetric collisions with a finite crossing angle. The BELLE detector is optimized to observe **CP** violation in B decays at KEKB. In this chapter, we will briefly describe the accelerator and the detector.

3.1.1 KEKB accelerator

The KEKB accelerator was designed to produce 10^8 $\Upsilon(4S)$'s per year, with a center-of-mass energy adjusted to the $\Upsilon(4S)$ resonance. The design luminosity is $10^{34} \mathrm{cm}^{-2}\mathrm{s}^{-1}$ which is the highest in the world.

Almost all the $\Upsilon(4S)$ mesons decay into B meson pairs. Since the threshold energy for the pair creation of B mesons is nearly equal to the mass of $\Upsilon(4S)$ which is 10.58 GeV, the momentum of each B is only 0.34 GeV/c in the $\Upsilon(4S)$ rest frame.

In order to mmeasure the decay time difference from the distance between B-decay vertices, therefore, $\Upsilon(4S)$ mesons need to be boosted so as to provide enough flight distance of B mesons. The Lorentz boost parameter is chosen to be $\beta\gamma = 0.425$.
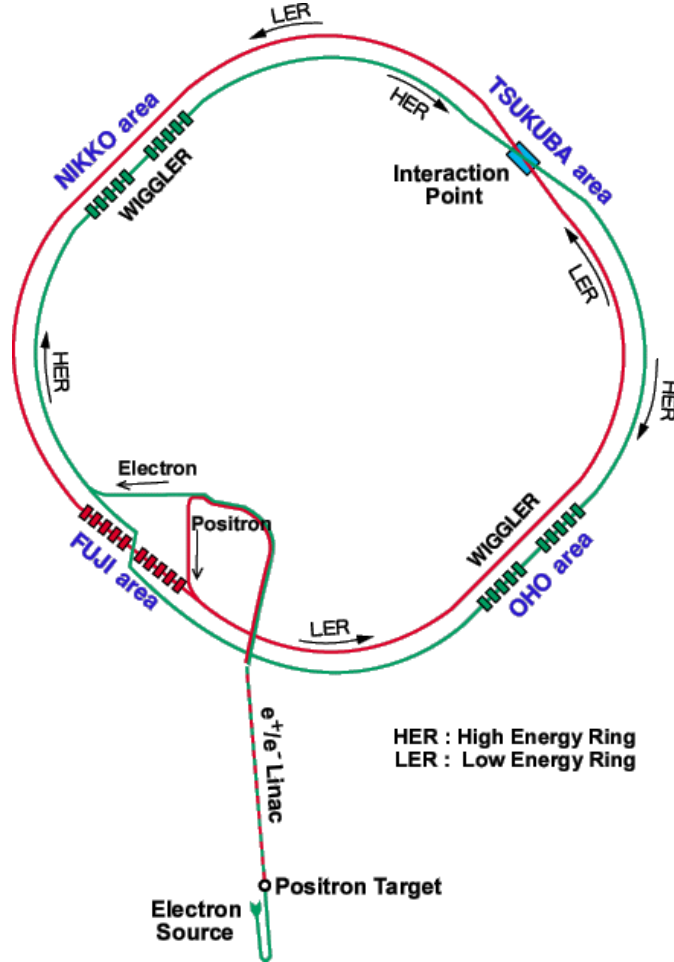
Figure 3.1: *Composition of the KEKB accelerator system.*

Figure 3.1 illustrates the KEKB acceralator system. It consists of 2 main rings, the HER (High Energy Ring) to keep electrons at 8 GeV and the LER (Low Energy Ring) to keep positrons at 3.5 GeV, and the LINAC to accelerate both electrons and positrons. Both electrons and positrons collide at the TSUKUBA area where the BELLE detector is placed. The main parameters of KEKB are listed in Table 3.1 [20].

Table 3.1: *Main parameters of KEKB.*

Ring		LER	HER	
Energy	E	3.5	8.0	GeV
Circumference	C	3016.26		m
Luminosity	$\mathcal{L}$	1×10^{34}		$\mathrm{cm}^{-2}\mathrm{s}^{-1}$
Crossing angle	θ_x	± 11		mrad
Tune shifts	ξ_x/ξ_y	0.039/0.052		
Beta function at IP	β_x^*/β_y^*	0.33/0.01		m
Beam current	I	2.6	1.1	A
Natural bunch length	σ_z	0.4		cm
Energy spread	σ_ε	7.1×10^{-4}	6.7×10^{-4}	
Bunch spacing	s_b	0.59		m
Particle/bunch	N	3.3×10^{10}	1.4×10^{10}	
Emittance	$\varepsilon_x/\varepsilon_y$	$1.8 \times 10^{-8}/3.6 \times 10^{-10}$		m
Synchrotron tune	ν_s	$0.01 \sim 0.02$		
Betatron tune	ν_x/ν_y	45.52/45.08	47.52/43.08	
Momentum compaction factor	α_p	$1 \times 10^{-4} \sim 2 \times 10^{-4}$		
Energy loss/turn	U_o	0.81†/1.5‡	3.5	MeV
RF voltage	V_c	$5 \sim 10$	$10 \sim 20$	MV
RF frequency	f_{RF}	508.887		MHz
Harmonic number	h	5120		
Longitudinal damping time	τ_ε	43†/23‡	23	ms
Total beam power	P_b	2.7†/4.5‡	4.0	MW
Radiation power	P_{SR}	2.1†/4.0‡	3.8	MW
HOM power	P_{HOM}	0.57	0.15	MW
Bending radius	ρ	9 16.3	104.5	m
Length of bending magnet	ℓ_B	0.915	5.86	m

†: without wigglers, ‡: with wigglers

3.1.2 BELLE detector

The structure of the BELLE detector is asymmetric due to the asymmetric beam energy of KEKB, as shown in Figure 3.2. The BELLE detector has 1.5 T superconducting solenoid and sub-detectors optimized to observe particles from B meson decays : the Silicon Vertex Detector (SVD), the Central Drift Chamber (CDC), the Aerogel Čherenkov Counter (ACC), the Time of Flight counter (ToF), the Electro-magnetic Cesium iodide caLorimeter (ECL) and the K_L and Muon detector (KLM).

These sub-detectors are grouped into two: i.e. tracking devices (the SVD, CDC) and particle identification devices (the CDC, ACC, ToF, ECL, KLM).[1] The definition of coordinate system is shown in Figure 3.3.

For muon identification, the CDC and the KLM are used. A muon with sufficient momentum can reach and penetrate the KLM, whereas other particles don't. Although a small fraction of pions can reach the KLM, it is largely scattered inside the KLM. Therefore muons can be clearly identified by checking the range and χ^2 of a reconstructed track in the KLM which is made by extrapolating the track in the CDC.

3.1.3 Status of Data Taking

The KEK B factory was commissioned and started taking data in 1999. The integrated luminosity recorded (as of January 2000) is 0.34 fb^{-1}, corresponding to more than 10^6 collision events with hadronic interaction.

3.2 Central Drift Chamber (CDC)

The Central Drift Chamber (CDC) has two important roles. One is to reconstruct charged tracks for measurement of momentum from its curvature, and the other is to measure energy loss (dE/dx) in the CDC, which depends on velocity ($\beta = v/c$). Therefore, the kind of particles can be specified with both information.

The CDC has a cylindrical shape with inner and outer radii of 8 and 88 cm, respectively. It consists of 50 sense-wire layers and 3 cathode strip layers. The sense-wire layers are grouped into 11 super layers : 6 axial and 5 stereo super layers. Stereo angles range from 42.5 mr to 72.1 mr. The number of readout channels is 8,400 for anode wires and 1,792 for cathode strips. A mixture of 50% helium-50% ethane gas is used in the chamber to

---

[1] the CDC is also used for particle identification since it provides dE/dX information.
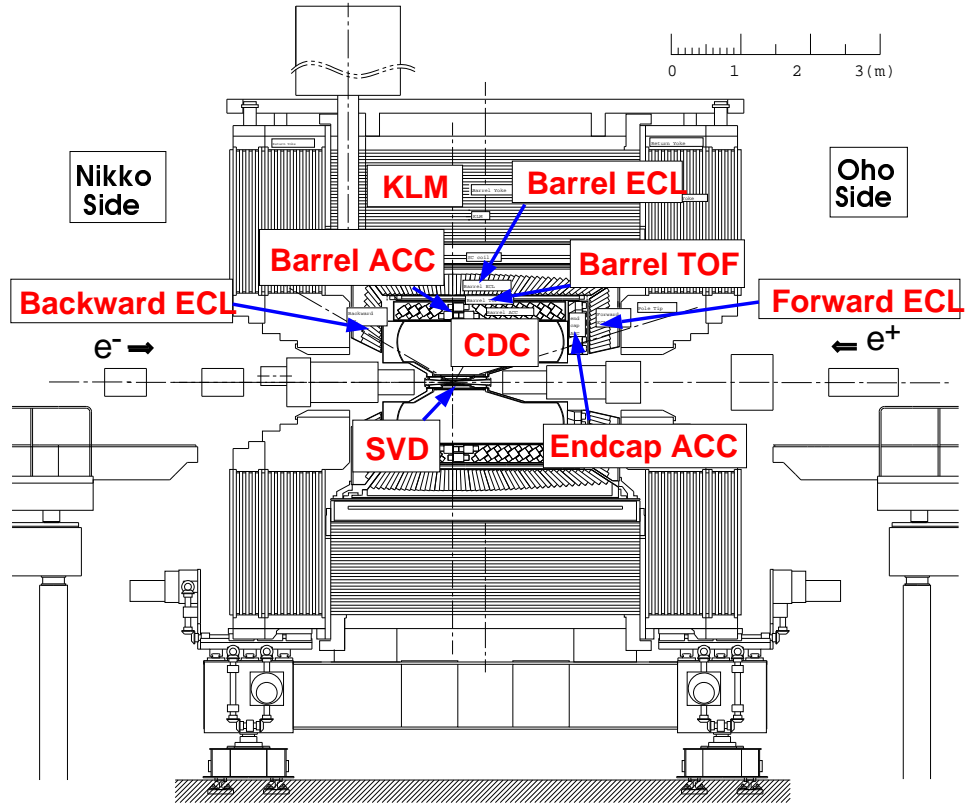
Figure 3.2: *Side view of the BELLE detector.*
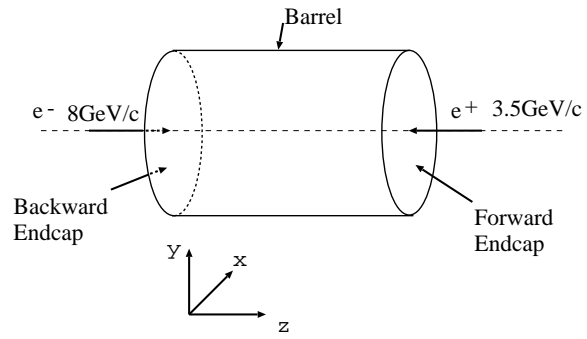
Figure 3.3: *The definition of the BELLE coordinate.*

minimize the multiple Coulomb scattering contribution to the momentum resolution. Figure 3.4 shows an example of an event display for the CDC.
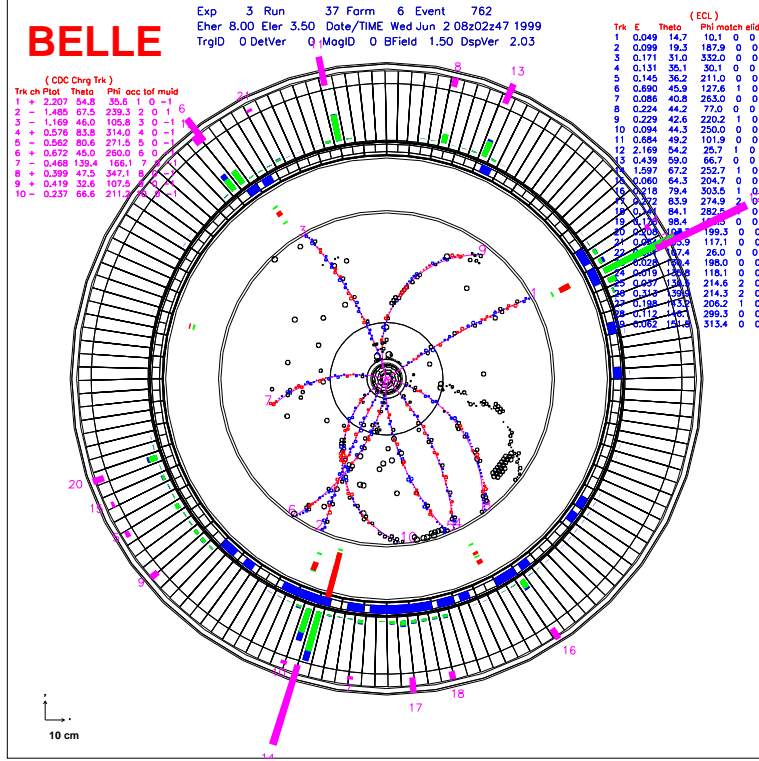
Figure 3.4: *An example of an event display for the CDC.*

3.3 K_L and Muon Detector (KLM)

The KLM is the outermost sub-detector of the BELLE. There are two main purposes of the KLM. One is K_L detection, and the other is muon identification. K_L mesons are an important since $B^0 \to J/\psi K_L$ can also be used to observe **CP** violation. As described in Chapter 2, muons are important because J/ψ decays to $\mu\mu$.
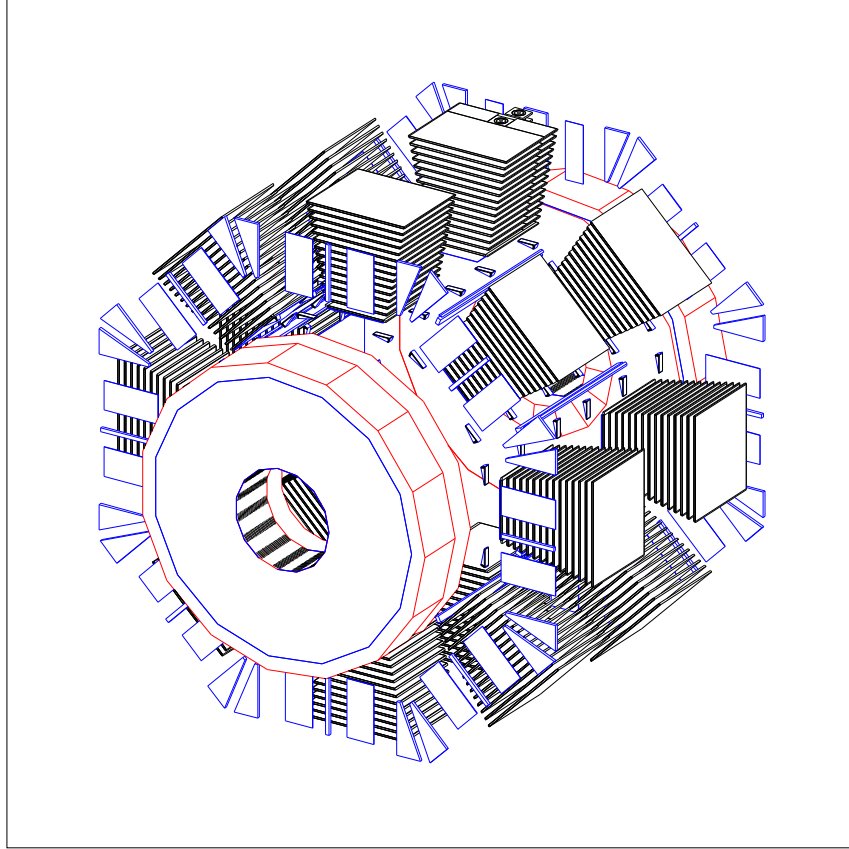
Figure 3.5: *BELLE KLM detector.*

3.3.1 Requirements for KLM

A large amount of material is required to stop and detect K_L and μ. Therefore the KLM consists multi-layers of absorbers and sensors. Requirements for the sensor layers are as follows :

1. To more absorbers thick enough, each sensor must be thin.

2. Since the KLM is outermost and the largest detector, it is desirable to be composed by inexpensive material as much as possible.

3. Each sensor should be simple for easy fabrication and maintennance. It must also be stable for a long-term operation.

4. To reconstruct K_L mesons and muons, high detection efficiency and sufficient position resolution are essential.

The KLM detector was designed to satisfy such requirements.

3.3.2 Structure of KLM

The KLM consists of one barrel and two endcap parts. An overview of the KLM is shown in Figure 3.5.

The octagonal barrel is segmented longitudinally into fifteen detector superlayers interleaved with fourteen 4.7 cm thick iron plates. The amount of iron corresponds to ~ 37 radiation length : i.e. the total amount reaches ~ 43 radiation length. A detector superlayer comprises two Resistive Plate Counters (RPC's) and copper strips to read out inner aluminum frame. The dimensions are 220 cm (length) $\times$ 151 $\sim$ 267 cm (width) $\times$ 3.9 cm (thickness).[2]

The longitudinal segmentation of the endcaps is identical to that of the barrel, except that the innermost detector layer is left out. An endcap superlayer module is shaped as a quarter sector extending radially from 130.5 cm to 331 cm.

The innermost forward (backward) RPC is at $z = 273$ cm ($z = -179$ cm), so that the nominal coverage in θ is from 24.3° to 145.5°. Endcap cathodes are segmented in θ and ϕ rather than x and y as illustrated in Figure 3.6.
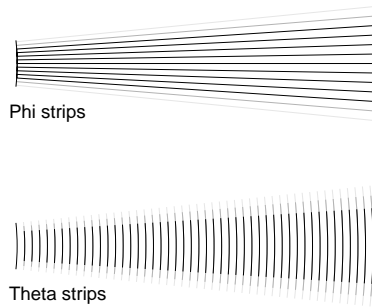
Figure 3.6: *Patterns of cathode strips for the endcap detectors.*

---

[2] The gap where each superlayer was inserted is 4.4 cm.

3.3.3   Resistive Plate Counter (RPC)

The RPC is a kind of spark chamber with the following properties :

- No amplifier is needed because of its large pulse height of ~ 100 mV.

- Good time resolution of ~ 2 nsec.

- It is easy to make large and complex shape.

- It is made of inexpensive material.
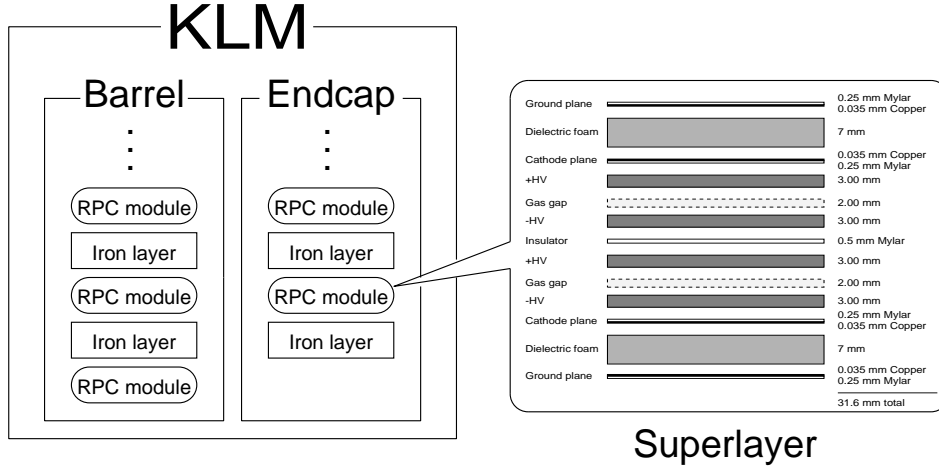
Figure 3.7: *The superlayer structure of KLM.*

The principle of the operation of RPC is as follows : When operated with a gas mixture of argon (61%), isobutane (35%) and Freon 116 (4%) in an electric field of 3.7–4 kV/mm in the 2 mm gap, a throughgoing charged particle initiates an avalanche in the gas. The positive ions in this avalanche draw more electrons out of the negative cathode, leading to a "spark" between the negative and positive cathodes. The high resistivity of the electrodes ($\rho = 10^{11\pm1}\,\Omega \cdot$ cm) prevents the rapid replenishment of the charge transferred in the spark, thus quenching the discharge. This process is known as a "limited streamer". After a few milliseconds, the plate in this 0.1 cm^2 dead region of the RPC becomes recharged as electrons bleed through the resistive electrodes, thus restoring the electric field. The isobutane absorbs UV photons, preventing significant afterpulsing. The streamer is imaged on

external cathodes that also act as transmission lines.[3] The leading edge of the 200 mV peak cathode signal has a resolution of 2 ns because of the small time jitter in the formation of the streamer.

An RPC module of the KLM has the superlayer structure as illustrated in Figure 3.7. As two RPCs in one module have strips perpendicular to each other, we can obtain 2-dimensional position information. The widths of cathode strips are $4.3 \sim 5.5$ cm in ϕ and 4.5 cm in Z for the barrel RPC modules, and 2.1 cm ~ 5.0 cm in ϕ and 3.8 cm in θ for endcaps. The intrinsic position resolution will be explained in detail in Chapter 5. The superlayer structure also gives redundancy for the hit detection. As the efficiency of a single RPC module is $\sim 90\%$, the superlayer module provides $\sim 99\%$ efficiency [9].

---

[3] No information about energy of charged particle is read out.

Chapter 4

Method of Muon identification

To detect a muon, first a charged track must be reconstructed in the CDC. Then, hits inside the KLM associated with the track should be found. However, these two conditions are not sufficient to reduce contamination from other kinds of particles. In this chapter, we describe how to reject such contamination while keeping high detection efficiency for muons.

4.1   Charged tracks entering KLM

Charged particles reconstructed in the CDC are electrons, muons, pions, kaons and protons. Except muons, most of the particles do not reach the KLM because of the electro-magnetic or hadronic interactions in the material of the inner detectors. Figure 4.1 shows the number of charged particles which reach the KLM in case of the $B^0 \bar{B}^0$ generic decays as well as their momentum distributions.

Pion Pions are the dominant source of the contamination. As shown in the table attached to Figure 4.1, the number of pion tracks reaching the KLM is about 4 times as large as muons. However, most of pions can be rejected with utilizing hadronic shower in detectors. Remaining "punch-through" pions and decay muons from pions will be described in the next section.

Kaon Kaons are the 2nd largest source of contamination. However, even though the number of kaons reaching the KLM is roughly the same as the number of muons, the ratio of the kaon mass to the muon mass is
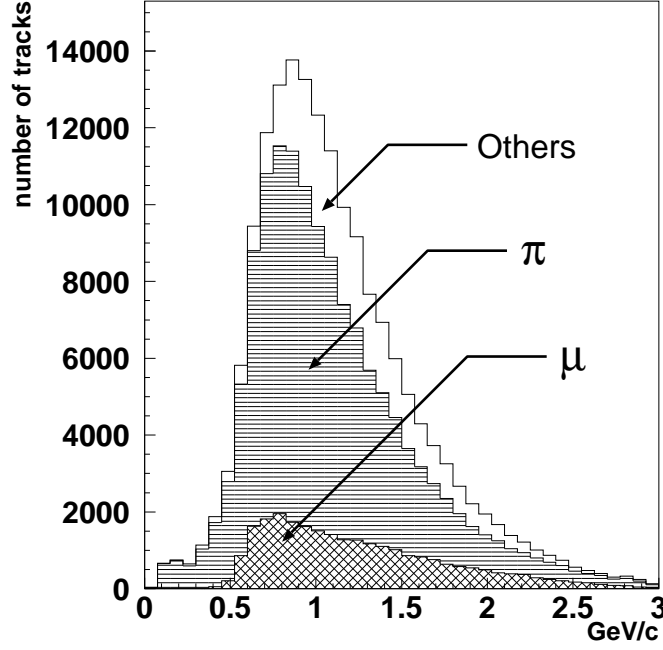
Particle kind		Number
muon		25984
pion		112043
others	kaon	31290
	electron	1331
	proton	1074

Figure 4.1: *Momentum distributions of charged particles which deposit energy in KLM.*
This plot was made by Monte Carlo simulation with 80000 $B^0\bar{B}^0$ events. Each particle kind is determined while it is passing the CDC. Therefore if a particle entering the KLM is a decay product, the particle kind of its parent is used.

large enough for the separation. Thus the contamination of kaons is very small.

Electron The number of electrons entering the KLM is much lower than the number of muons, and is about one twentieth. Also the probability of bremsstrahlung is much larger, since it is proportional to the half power of the mass and $m_\mu : m_e = 207 : 1$.

18

Proton The number of protons is roughly the same as that of electrons. Furthermore, its mass is about 10 times as large as the mass of muons. Therefore the contamination by protons can be almost ignored.

In conclusion, the contamination except pions can be almost ignored. Thus in the following sections only pions are considered as the source of the contamination.

4.1.1 Classification of prompt muons
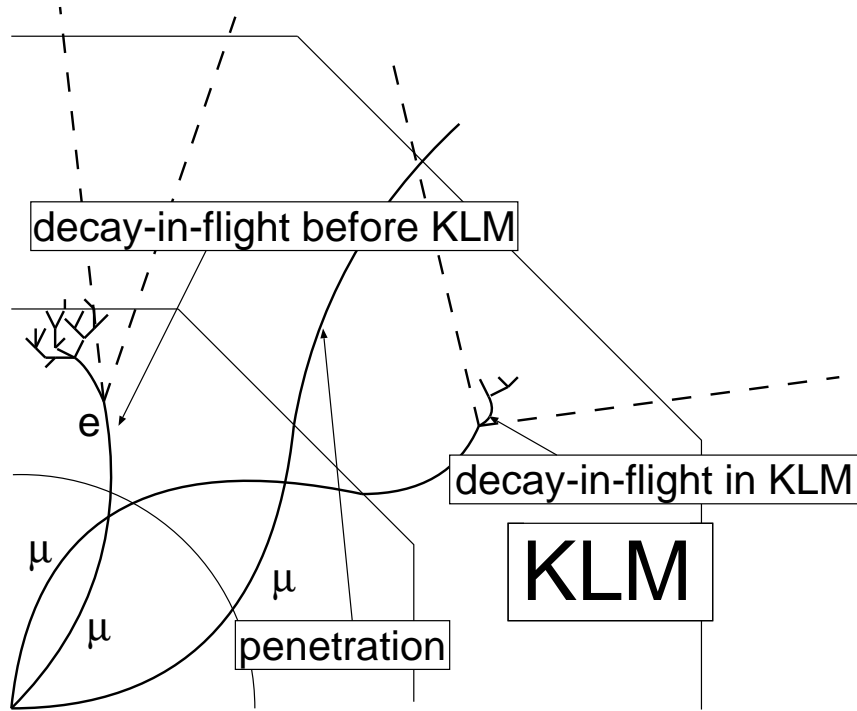
Figure 4.2: *Various prompt muons in KLM.*
Prompt muons are classified into "decay-in-flight in front of KLM", "decay-in-flight in KLM" and "penetrating muons which don't decay nor stop in KLM".

Several types of muons are seen in the KLM. What is really important is the muons produced close to the interaction point, such as the cases $J/\psi \to \mu\mu$ and $B \to D^*\mu\nu$. In this thesis, such muons are defined as "prompt muons". Prompt muons are sorted in 3 classes. After passing the CDC, a part of

muons decay into electrons in front of the KLM. Such muons are defined as "decay-in-flight muons before KLM". Furthremore, some muons decay inside the KLM (most of them stop in detector components). They are defined as "decay-in-flight muons in KLM". Remaining muons which penetrate the KLM are defined as "penetrating muons". This classification is illustrated in Figure 4.2. Their momentum distributions with single-track Monte Carlo simulation are shown in Figure 4.3.
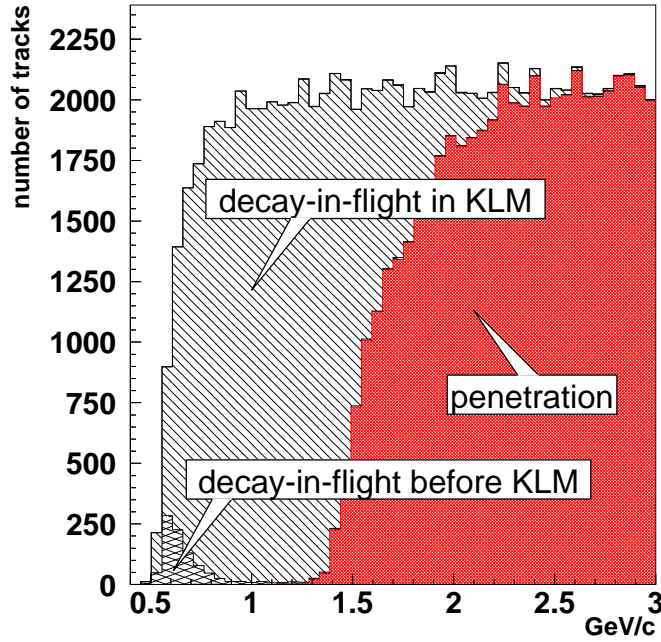
Figure 4.3: *Classification of prompt muons.*
This plot was made by Monte Carlo simulation about single muon tracks.

This plot can be summarized as follows :

- Most of prompt muons reach the KLM without decaying in flight.

- Available lower limit of momentum is about 0.5 GeV/c.

- Most of prompt muons with momentum below 1.5 GeV/c decay in-flight inside the KLM.

- In higher momentum region, almost all the prompt muons penetrate the KLM.

4.1.2 Classification of prompt pions
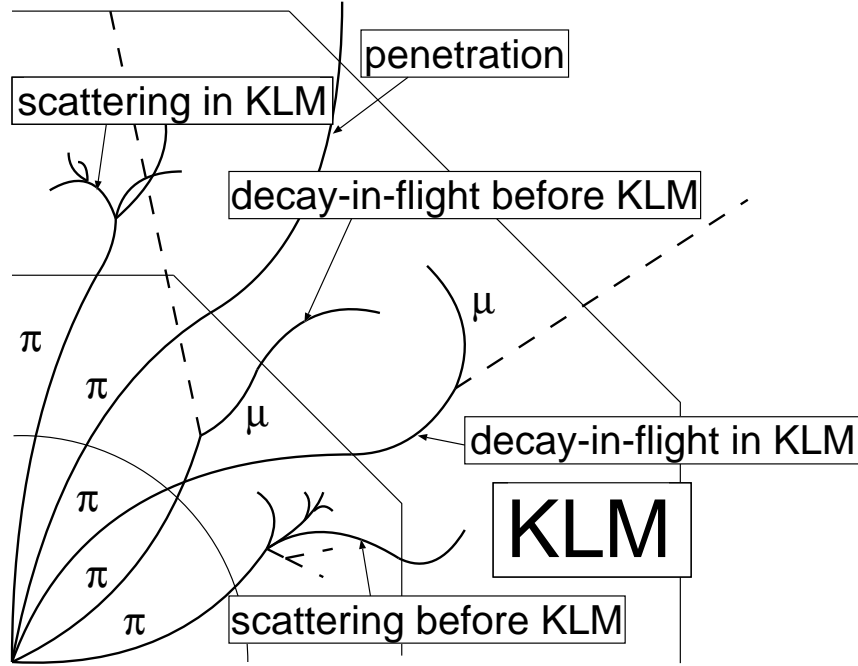
Figure 4.4: *Various prompt pions in the KLM*
The classification of prompt pions are similar to muons. i.e. "decay-in-flight in front of KLM", "decay-in-flight in KLM", "penetrating KLM without decaying". Furthermore, products from "scattering of prompt pions with material in front of KLM" (including scattered pions and muons which are it s decay products) and "scattered products but interacted at inner KLM".

Prompt pions can be categorized as a similer way to prompt muons. Decay-in-flight pions before or in the KLM, and penetrating pions are also defined. In case of pion, however, hadronic interactions have to be considered also. Most of pions are scattered with nucleus in material before the KLM, and its daughters, which include muons decaying from scattered pions, enter the KLM. A part of pions also scatter in the KLM. This classification is illustrated in Figure 4.4. Their momentum distributions with single-track Monte Carlo simulation are shown in Figure 4.5.

This plot can be summarized as followings :
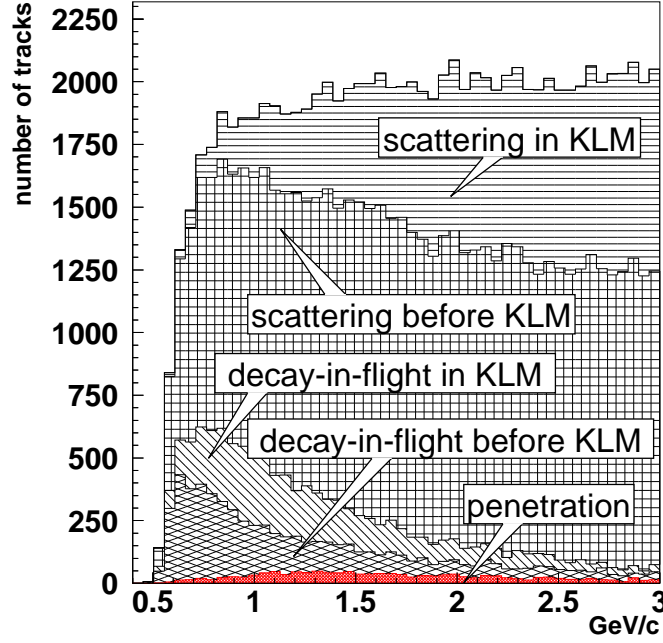
Figure 4.5: *Momentum distributions of prompt pions*
This plot was made by Monte Carlo simulation about single pion tracks.

- Most probable process is "scattering before KLM".

- In the lower momentum region (especially below 1 GeV/c), decay-in-flight pions become more significant.

- In the higher momentum region, the fraction of scattering inside the KLM increases.

- Penetrating pions are much smaller than the case in prompt muons, but distribute almost uniformly.

- Available lower limit of momentum is about 0.5 GeV/c which is the same as prompt muons.

Evident differences are seen between muons and pions. Therefore, if we utilize above features, we can separate pions from muon candidates.

4.2 Parameterization of "good" Muon

Some variables are defined here to separate prompt muons from sources of contamination, which lead to parameterization of "good" muons.

As already mentioned, muons can penetrate many layers. Hence, the number of penetrated RPC layers is an useful index. However Figure 4.3 and 4.5 indicate that not all of muons penetrate the KLM, whereas even some pions can penetrate it like muons. Therefore we need another index to represent the behaviour of muons.

Consider what happens when a prompt pion interacts with nucleus in the detector with hadronic interaction. Because of large scattering angles, many hits generated by the pion are far from expected position for muon, and the measured range in the KLM also becomes shorter than expected. This is illustrated in Figure 4.6.
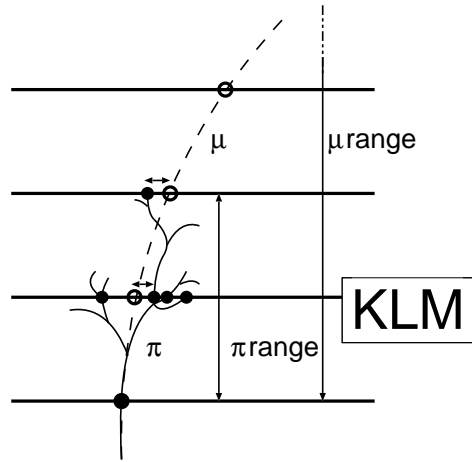
Figure 4.6: *Pions scattered inside KLM.*

Since χ^2 can justify whether its distribution is correct or not, the combined information of measured range and χ^2 about reconstructed trajectory is the most useful index. In this study, χ^2 is calculated by each hit associated with the reconstructed track and the range is measured by the outermost layer which an associated hit.

Figure 4.7 shows the distribution of χ^2 and range obtained by single track Monte Carlo simulation. The distribution of χ^2 has a sharp peak around 1 in the case of muons. On the other hand, χ^2 for pions has much broader distribution than muons. Just an opposite tendency is seen between muons
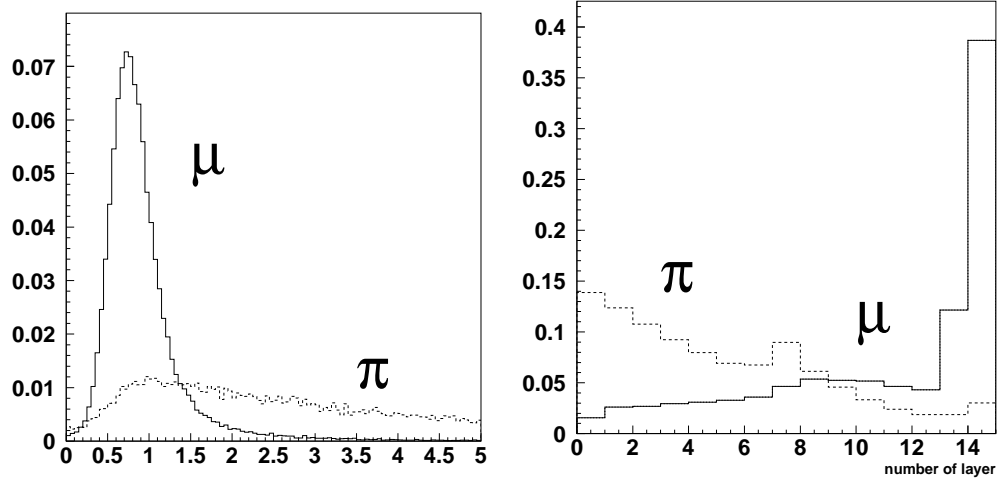
Figure 4.7: χ^2 and range distributions for muons and pions.
Left: reduced χ^2 distribution,
Right: measured range distribution.
Both plots are made by single track Monte Carlo simulation.

and pions for the range distribution. Both plots prove that they are useful to describe "good muons", so as to separate muons and pions.

4.3 Muon identification procedure

In order to obtain χ^2 and range, a muon candidate should be reconstructed as precise as possible. We can use RPC hits as inputs for track reconstruction. Charged tracks which are reconstructed in the CDC are extrapolated to the KLM with an extrapolator using the GEANT [15] program, then they are considered as muon candidates. An usual method utilized by BELLE was as follows :

1. extrapolate a muon candidate with a GEANT-like extrapolator,

2. include multiple Coulomb scattering effect as covariance of tracking parameters, position and momentum,

3. open a "window" proportional to the covariance and associate hits which exist in the "window",

24

4. measure the residual of extrapolated position and associated hits, then calculate χ^2 ,

5. iterate this process,

6. finally measure range and compare with expected range based on muon assumption,

7. identify the muon with applying cuts to obtained values.

This method is effective to a certain extent, if covariance is correctly estimated.

4.3.1 "Blind" extrapolation
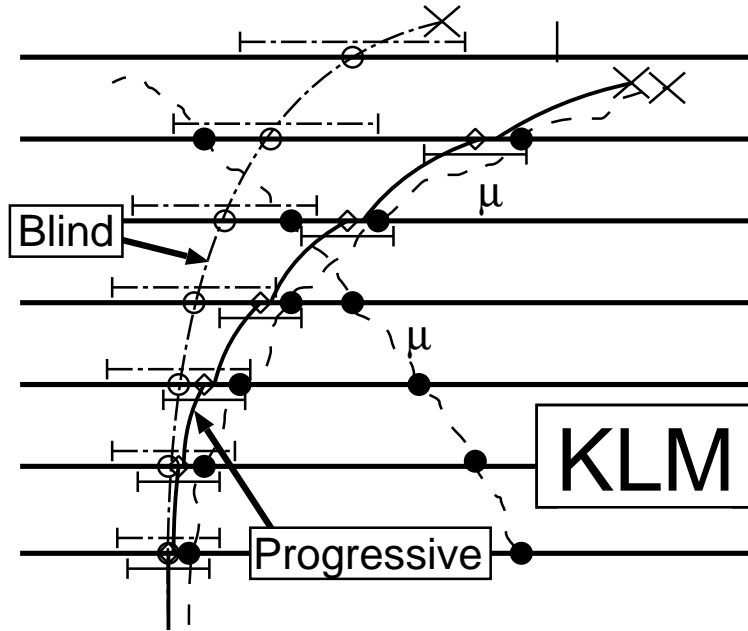
Figure 4.8: *The scheme of track reconstruction for muon candidates.*
A muon trajectory is shifted by multiple Coulomb scattering. Blind extrapolation may lose hits, includes fake hits generated by another track or noise, or results in a wrong range. Progressive extrapolation may correctly follow this on the other hand.

In the usual method described above, the quality of the fit becomes worse with an unexpected large-angle scattering or a pile-up of many small-angle scattering.

That's why this method is called "blind extrapolation". Of course if we enlarge the search window which is proportional to the covariance matrix, we may take many RPC hits. However, such a wide window allows to include fake hits which are made by another candidate, or shower of neutral hadrons, or just noise. On the other hand, if we reduce the window size, we lose some RPC hits. Then calculated results are no longer accurate.

4.3.2 "Progressive" extrapolation

If we include information of each hit layer by layer, after one hit is associated, the track itself is updated with this information and the last status. Then, the next extrapolation point is predicted. If this process is iterated, all the hits can be included one after another. This method is called "Progressive extrapolation". Figure 4.8 shows this scheme.

It is sufficient for progressive extrapolation to have a relatively narrower window, since extrapolated position is close to reality. Even if unexpected phenomenon occurs, the updated track with this information may predict the next position. This fact gives an additional merit. Because an extrapolated track is closer to material which is passed by the real muon, energy loss is more correctly estimated. Consequently, range is more precisely calculated.

One of effective methods for progressive extrapolation is the Kalman filter. Kalman filter is an all-purpose theory which originates from system theory as a mean of analyzing a discrete linear dynamic system. This method is already adopted by track filtering in SVD [14] and fitting in CDC. Kalman filter theory and its application to the KLM is mentioned in the next chapter.

4.3.3 Muon identification

In this study, muon identification is done with only three cut parameters. All parameters depend on range or χ^2 which are discussed already.

number of associated layer The number of associated layer is the number of RPC layers which are associated with an extrapolated track. It is used for low momentum pion reduction.

range difference Range difference means the difference between the outermost hit-layer expected by muon assumption and the measurement.
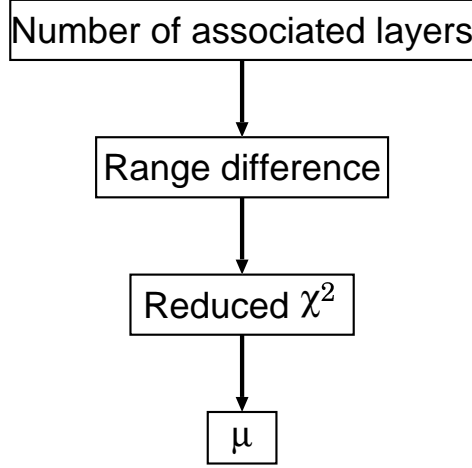
Figure 4.9: *The flow of muon identification.*

In case of muons, it is expected to be close to 0. On the otherhand, if it is a pion, the value will be spread.

reduced χ^2 As well known, though the expected value of χ^2 shifts depending on the degree of freedom, reduced χ^2 which is divided by the degree of freedom is around 1 in average. That is why reduced χ^2 is used as a cut parameter. Since RPC read out consists of two strips crossing perpendicularly, a reconstructed hit has 2 degrees of freedom. Consequently, χ^2 is divided by twice of the number of reconstructed hits. This fact implies that it depends on momentum, as the number of hits depends on momentum also. Therefore, we introduce a momentum dependent cut.

These cut values are applied to muon candidates in the order shown in Figure 4.9. Only a muon candidate which passes all the cuts is considered as a muon.

Chapter 5

Kalman Filter

The Kalman filter is the most popular tool for track fitting in high energy physics experiments today [11, 12, 13] and it has been successfully implemented for LEP experiments, CLEO and BELLE. In this chapter, principles of Kalman filter and its application to the KLM are described.

5.1 Principles

The Kalman technique focuses on a $p \times 1$ **state vector** that contains the p state parameters to be estimated, and on a **model** that extrapolates the state vector from point to point. These points can either be real points in space or time, or can simply be dimensionless integers (e.g. the track number in vertex fitting).

In the following, we use $\bar{\alpha}_k$ to denote the $p \times 1$ state vector containing the true state parameters at point k. The state vector extrapolation model in the linear case is :

$$\bar{\alpha}_k = F_{k-1}\bar{\alpha}_{k-1} + w_{k-1} \tag{5.1}$$

where F_{k-1} is a matrix that extrapolates the state vector from point $k-1$ to point k and w_{k-1} represents "process noise" that corrupts the state vector (in track fitting, for example, the process noise is due to multiple scattering). The process noise is assumed to be unbiased and to have finite variance, and its covariance matrix is Q_k.

The components of the state vector $\bar{\alpha}_k$ are not measured directly. The actual m measurements m_k at point k are linear functions of the state vector $\bar{\alpha}_k$ such that,

$$m_k = H_k\bar{\alpha}_k + \varepsilon_k \tag{5.2}$$

where m_k is a $m \times 1$ vector, H_k is a $m \times p$, and ε_k represents measurement noise, or measurement errors. In analogy to the process noise, the measurement noise ε_k is assumed to be unbiased and to have finite variance, and its covariance matrix is V_k. Overview of this system is illustrated in Figure 5.1.
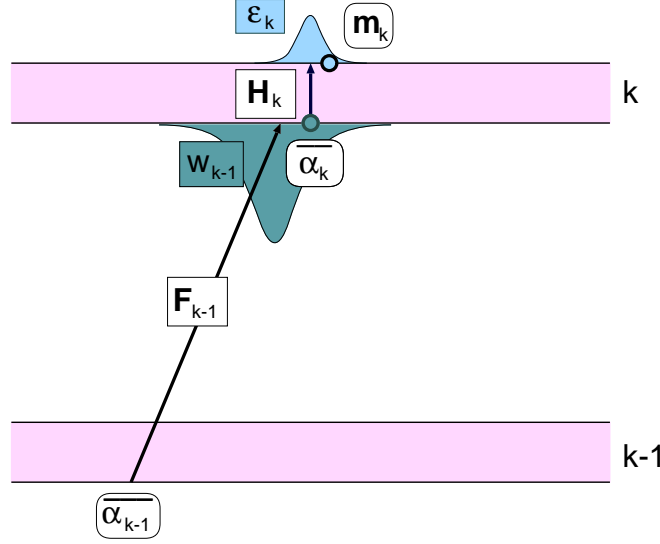
Figure 5.1: *Dynamic system for this study.*
The state vector at point k-1, $\bar{\alpha}_{k-1}$ is extrapolated by linear transformation F_{k-1}, with process noise which obeys Gaussian distribution. Actual mesuarements m_k at point k comes from projecting $\bar{\alpha}_k$ by matrix H_k, with smearing by measurement noise ε_k.

Then we define α_k^{k-1} to be the best estimate of the true state vector $\bar{\alpha}_k$ using all measurements up to but not including the k-th measurement, and α_k^k to be the best estimate of the state vector including the k-th measurement. In the language of Kalman filtering, α_k^{k-1} is the **predicted estimate** of $\bar{\alpha}_k$, and α_k^k is the **filtered estimate** of $\bar{\alpha}_k$. Further, for $n > k$, α_k^n is called the **smoothed estimate** of $\bar{\alpha}_k$.

In the Kalman scheme, α_k^k is taken to be arbitrary linear function of the extrapolated (or predicted) value of the state vector, α_k^{k-1}, and the actual measurement m_k made at point k :

$$\alpha_k^k = K_k^1 \alpha_k^{k-1} + K_k^2 m_k \tag{5.3}$$

where K_k^1 and K_k^2 are arbitrary matrices. The Kalman prediction equation is taken to be :

$$\alpha_k^{k-1} = F_{k-1}\alpha_{k-1}^{k-1} \tag{5.4}$$

Requiring α_k^k to be unbiased (i.e. expectation value of $(\alpha_k^k - \bar{\alpha}_k = 0)$) yields :

$$\alpha_k^k = \alpha_k^{k-1} + K_k(m_k - H_k\alpha_k^{k-1}) \tag{5.5}$$

where K_k is called the Kalman gain matrix and $r_k^{k-1} \equiv m_k - H_k\alpha_k^{k-1}$ is the predicted residual. Further,

$$K_k^1 = (I - K_kH_k) \tag{5.6}$$

and

$$K_k^2 = K_k \tag{5.7}$$

K_k is determined by requiring that it minimizes the sum of the squares of the standard deviations of the estimated parameters,

$$\frac{\partial Tr(C_k)}{\partial K_k} = 0 \tag{5.8}$$

where $Tr(C_k)$ is the trace of C_k and C_k is the $p \times p$ covariance matrix of the estimated parameters at point k. Solving for K_k yields :

$$K_k = C_k^{k-1}H_k^T(V_k + H_kC_k^{k-1}H_k^T)^{-1} \tag{5.9}$$

where

$$C_k^{k-1} = F_{k-1}C_{k-1}^{k-1}F_{k-1}^T + Q_{k-1} \tag{5.10}$$

and

$$C_k^k = (I - K_kH_k)C_k^{k-1} \tag{5.11}$$

The filtered residual r_k is derived from predicted residual :

$$r_k \equiv \alpha_k^k - \alpha_k^{k-1} = (I - H_kK_k)r_k^{k-1} \tag{5.12}$$

The covariance matrix of the filtered residual R_k becomes :

$$\begin{aligned} R_k &= (I - H_kK_k)V_k \\ &= V_k - H_kC_kH_k^T. \end{aligned} \tag{5.13}$$

χ^2 incremments :

$$\chi_k^2 = \chi_{k-1}^2 + r_k^T R_k^{-1} r_k. \tag{5.14}$$

$\mathbf{m}_k$

α_k^{k-1}

$\mathbf{H}_k$

k

$\overline{\alpha_k}$

$\mathbf{F}_{k-1}$

k-1

α_{k-1}^{k-1} $\overline{\alpha_{k-1}}$

Residual

$\mathbf{m}_k$

α_k^k

$\mathbf{H}_k$

k

α_k^{k-1}

K

$\overline{\alpha_k}$

k-1

α_{k-1}^{k-1} $\overline{\alpha_{k-1}}$
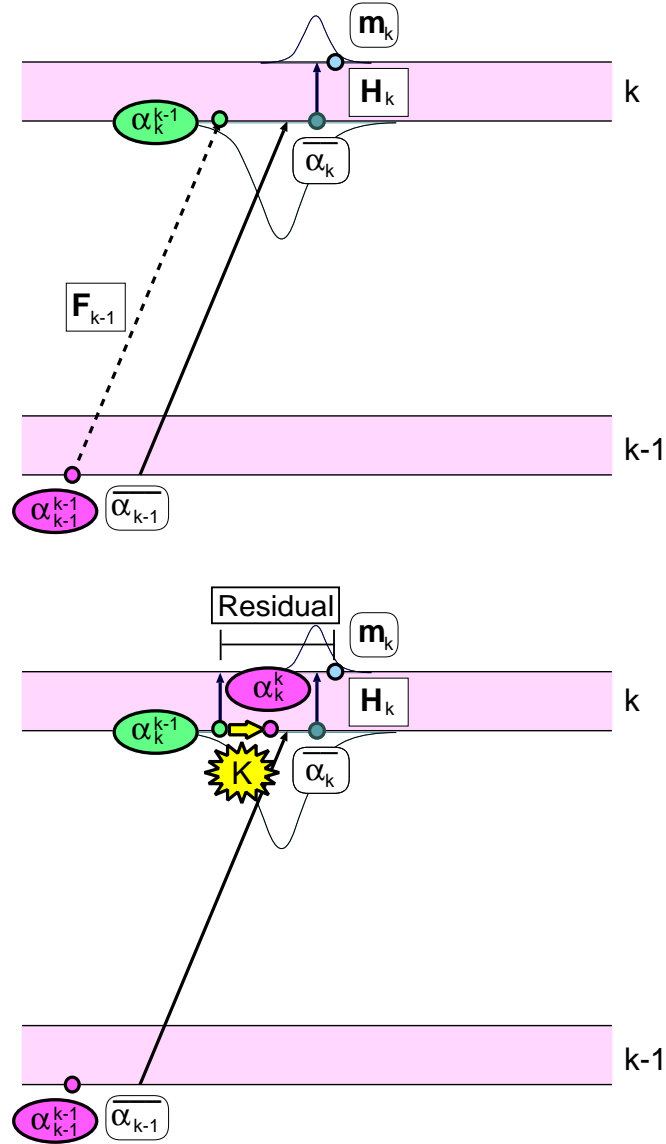
Figure 5.2: *The scheme of Kalman filter.*
Upper: prediction of state vector, Lower: filtering of predicted state vector.
Estimated state vector up to k-1 is extrapolated by linear transformation
matrix same as true state vector. This operation is called "prediction".
After that, predicted state vector is projected to predicted measurement. It
is compared by actual measurement, then Kalman gain is calculated with
its residual. Kalman gain updates predicted state vector to latest estimated
state vector. This operation is called "filtering".

(the superscript T denotes the transpose). In correspondence to our earlier notation, C_k^{k-1} is the best estimate of C_k excluding the k-th measurement, and C_k^k is the best estimate of C_k including the k-th measurement. These schematic views are shown in Figure 5.2 We note that our equations correspond to the "gain matrix" formulation of the Kalman filter method. Frühwirth further explores the "weighted means" formulation, focuses on the K_k^1 and K_k^2 matrices instead. The two methods are mathematically equivalent; the gain matrix formulation is generally preferred if $m < p$.

5.2 Application of Kalman filter to KLM

In order to implement Kalman filter to a real detector, we have to decide the following 3 points :

- initial state vector to start Kalman filter ($\bar{\alpha}_0$).

- extrapolator to move state vector from one measurement point (F_{k-1}) to the next point.

- actual measurement quantities to update the state vector.

In this section, these items are described for the case of the KLM.

5.2.1 Initial state vector

The Kalman filter requires a starting state vector. In the BELLE environment, this is achieved as the result of tracking performed in the CDC and the SVD. To begin with, tracks are reconstructed in the CDC and expressed by helix parameters which are convenient to describe helical trajectories in a static magnetic-field. After that, they are updated with the SVD hits, utilizing a Kalman filter method. Then, these tracks are extrapolated from outer hits of the CDC to outer detectors by the GEANT [15]-like extrapolator which is employing GEANT routines internally. As a result, if an extrapolated track reaches the KLM, we can utilize this as the input for Kalman filter. Note that for the state vector, instead of a helix representation used in the CDC, we use the position-momentum vector (or any linear combination of these parameters). Since there is no magnetic field inside RPCs (cf. Figure 5.3), helix parameters can not be handled. Of course the covariance matrix is also transformed from helix parameters to position-momentum notation.
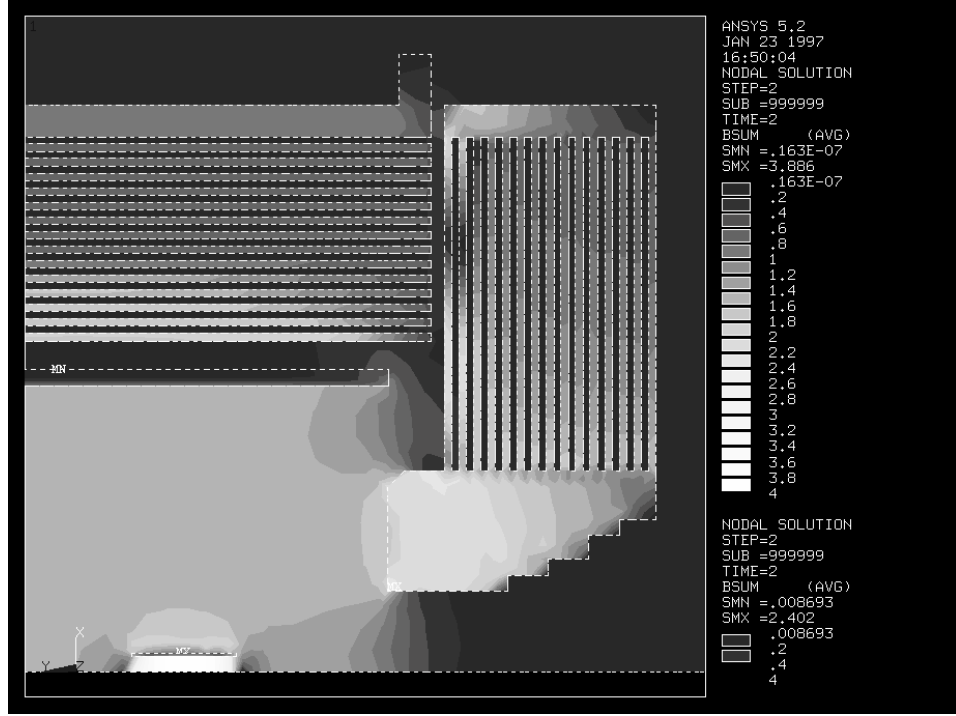
Figure 5.3: *Magnetic field in the KLM detector.*
The KLM iron absorber serves as a return yoke. Therefore it shows complex magnetic field with a strong dependence in polar angle or radius. In this plot, upper left structure is the KLM barrel region, right structure is the forward endcap region, lower parts are inner detectors and solenoid coil (the biggest black box between the KLM and inner parts). In the white areas the strongest magnetic field exists. In the KLM region, white boxes represent iron layers. Black boxes which are seen between iron layers are RPC layers. RPC layers have no magnetic field. These magnetic fields were measured before the experiment was started.

5.2.2 Extrapolator

Extrapolator is the model which is in charge of transportation of the state parameters between each hit included. In the case of the CDC, the Kalman filter procedure uses a simple helix and error matrix is updated one time for each step. However, in our case we just use the GEANT routines to perform the extrapolation between two layers and update the error matrices.

GEANT is the program that transport particles through the various regions of the setup, taking into account geometrical volume boundaries and physical effects according to the nature of the particles themselves, their interactions with matter and the magnetic field. In the non-uniform magnetic field, charged particles are transported using Runge-Kutta method for solving the kinematic equations.

We choose it for several reasons :

- In the CDC and the SVD, the material (e.g. SVD DSSDs, covers or the CDC gas) in question can be approximated by thin layers. Treatment of thin layers is straightforward in the update of the error matrix. The material in the KLM (materials of RPC + 4.7 cm of iron) is too thick to do the same thing. The effect of energy loss and multiple Coulomb scattering can not be taken into account in one step, and it must be divided in many steps until the thin layer assumption becomes acceptable.

- In the CDC and the SVD, the non uniformity of the magnetic field is taken into account as a correction. For the KLM, however, it is far more complex due to the fact that iron part is the return yoke and gives some large dependence in polar angle and radius of the magnetic field (cf. Figure 5.3).

- Although GEANT routines are rather time-consuming, the number of tracks reaching the KLM is small. Also in many cases extrapolation can be terminated in the middle as the particle may stop in the KLM. Therefore the time consumption is not an issue.

GEANT is the best candidate because it offers simplicity and excellent precision.

5.2.3 Measurement quantities

Kalman filter can deal with any quantities to update the state vector. In case of the KLM, RPCs give 2 dimensional hit position. Since 2 RPC strips are not placed on the same plane, reconstructed hit position is at the center of RPC. However, large resolution of RPC strip ($\sim 2cm$) dilutes this effect and we can assume that 2 strips are on the same plane. Figure 5.4 illustrates the schematic view of reconstruction of each hit.

In case multi-strips are fired, position is reconstructed as a center of gravity. Such multiplicity and its effect to the intrinsic resolution is studied
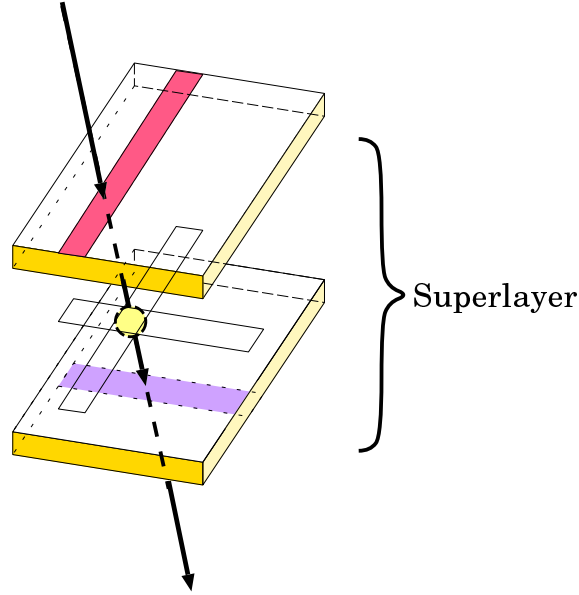
Figure 5.4: *Schematic view of a reconstructed hit*
A KLM superlayer has 2 RPCs and strips which are put on each end. When a charged particle penetrates it, each strip fires and gives one dimensional position. The crossing point of the hit strips gives the 2-dimensional position information.

with several ways. Figure 5.5 represents the multiplicity at the KLM detector and its effect to resolution. Though hits with high multiplicity make resolution worse, the fraction of such tracks is considerably small.

Table 5.1 shows the intrinsic resolution used in our Kalman filter. These values are obtained in the calibration runs with cosmic ray events.
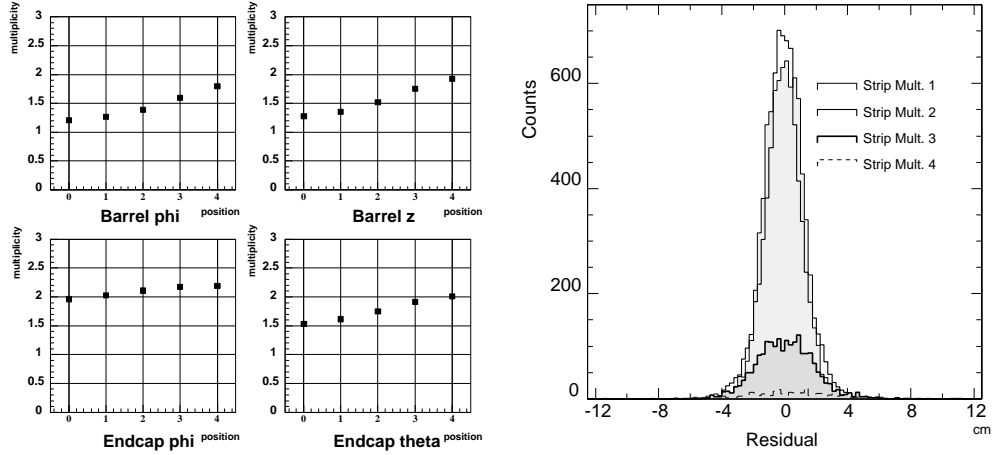
Figure 5.5: *Multiplicity and residual.*
Left: Average multiplicity distributions at several positions.
Right: Residual distributions for different multiplicities.
These quantities are obtained by cosmic ray calibration. Position 0-4 are arbitrary strips in order from inside to outside. In the barrel part, the mean multiplicity is about 1.5. On the other hand, endcap ϕ strips show rather higher multiplicity but still smaller than 3. Since 1 or 2 multiplicity cases show good resolution, hit multiplicity does not give so much impact on reconstruction 2 dimensional hits.

Number of strips	Barrel		Endcap	
	ϕ strip (cm)	z strip (cm)	ϕ strip (radian)	θ strip (cm)
1 strip	1.3	1.1	1.0	1.2
2 strips	1.3	1.1	1.1	1.4
3 strips	2.0	1.7	1.3	1.8
4 strips	3.3	2.9	1.7	3.0
n strips$(n \geq 5)$	$\sqrt{n/12} \times$ width of strip			

Table 5.1: *Intrinsic resolutions as a function of the numbers of hit strips.*

5.3 Basic Performance check

5.3.1 Definition

Residual

The definition of residual is the difference between the position of the track extrapolated to one RPC layer and the reconstructed hit :

$$\text{residual} = V_{\text{exp}} - V_{\text{hit}}, \tag{5.15}$$

where V_{exp} is the position of extrapolated track, V_{hit} is the position of the reconstructed hit. It is measured along each direction of RPC strip.

Pull

Pull is defined by the following formula :

$$\text{pull} \equiv \frac{R}{\sigma}, \tag{5.16}$$

where R is residual, σ is the standard deviation of track parameters. Therefore the pull should be unity if the error estimation is correct. The standard deviation σ consists of two parts : One (σ_{track}) comes from tracking quantities, which are handled by extrapolator(e.g. pposition-momentum). The other is measurement quantity σ_{meas}, which is measured by each active detector. Then, the total σ is

$$\sigma = \sqrt{\sigma_{track}^2 + \sigma_{meas}^2} \tag{5.17}$$

Reduced χ^2

This value was already mentioned in the previous.
χ^2 itself was defined in Function (5.14).

Range difference

Although range itself was already explained, it is effective to define a new parameter for comparison between muon assumption and reality.

$$\text{range difference} = \text{expected range} - \text{measured range} \tag{5.18}$$

If the candidate in question is a prompt muon, ideally speaking this index should be 0. For pions, the distribution will have a long tail.

5.3.2 Result

Tracking performance is first studied with single track Monte Carlo simulation. Each event contains a muon or pion single track with conditions listed in Table 5.2.

We compared progressive extrapolation (Kalman filter) with blind extrapolation. There was no other difference between two programs except the method of extrapolation.

Residual

The residual distributions are shown in Figure 5.6. In case of the blind extrapolation, because of multiple Coulomb scattering or inaccuracy of the reconstruction in the CDC, the position at the outermost layer is spread from true position and residual distribution shows large tails. The distribution for pions is rather similar. Consequently, large search windows are necesserly to hold high efficiency, which also allows many hits to be included for pions as well. On the other hand, Kalman filtering enables us to reduce it. The standard deviation of the residual becomes almost 2 cm which is a half of the typical strip width.
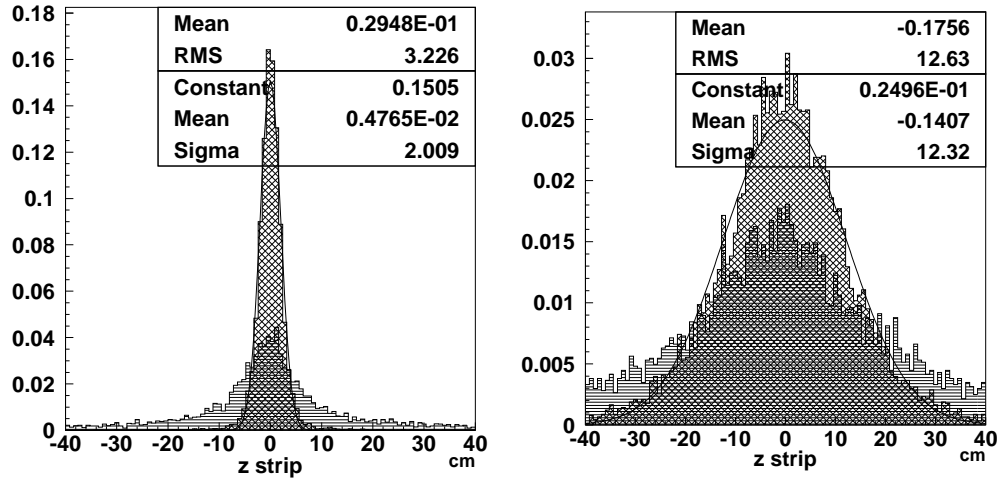
Figure 5.6: *The residual distributions with Kalman filtering (left) and with blind extrapolation (right).*
In each plot, a crossed histogram is for muons and the histogram filled with horizontal lines is for pions. These values are measured at the outermost layer, which had associated hits.

Pull

The pull distributions are shown in Figure 5.7. Though covariance is slightly overestimated in blind extrapolation (pull is 1.13), it is fixed by Kalman filtering, i.e. pull is nearly equal to 1. Therefore, error estimation in Kalman filtering is confirmed to be almost correct. In addition, this Gaussian tail proves that 6 σ window is sufficient, since almost all the muons are contained in this window. Pull for pions is largely stretched on the otherhand. It means that error estimation which is based on muon assumption is too small for pions.
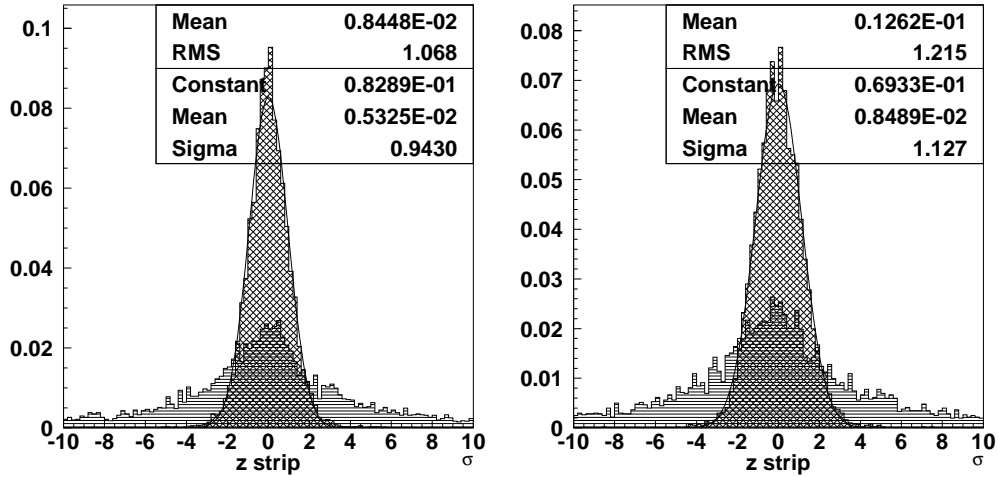
Figure 5.7: *The pull distributions with Kalman filtering (left) and with blind extrapolation (right).*
In each plot, a crossed histogram is for muons and the histogram filled with horizontal lines is for pions. These values are measured at the outermost layer which had associated hits.

Reduced χ^2

The χ^2 distributions are shown in Figure 5.8. The reduced χ^2 distribution is quite different between Kalman and blind extrapolation. The distribution with blind extrapolation shows a large tail. This is due to overestimation of covariance, lack of the care for large angle scattering, and poor reconstruction or extrapolation. The pion distribution for pions is also distorted. As a result, μ /π separation is not so effective. On the other hand, the peak

39

for muons is nearly equal to 1 with Kalman filtering. Pion contamination roughly shows flat distribution. This implies that pions can be correctly separated from muons.
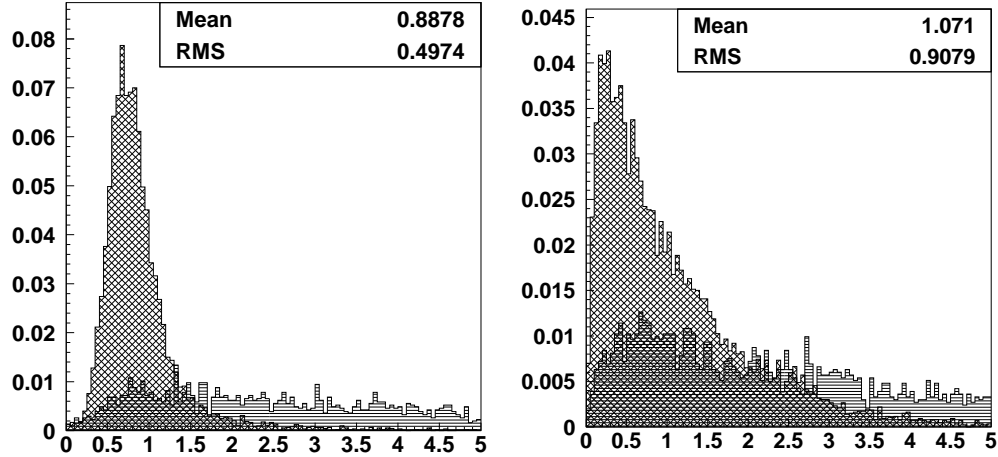
Figure 5.8: *The reduced χ^2 distributions with Kalman filtering (left) and with blind extrapolation (right). In each plot, a crossed histogram is for muons and the histogram filled with horizontal lines is for pions.*

Range difference

The range differences are shown in Figure 5.9. Range difference is expected to be 0 for muon. For blind extrapolation, 88% realize it, but others spread slightly wide. With Kalman filtering, such tracks are recovered. Almost 94% tracks just stop in the same layer as expected with smaller scattering. For both cases, pion distribution is clearly separated and more pions are rejected with Kalman filtering.
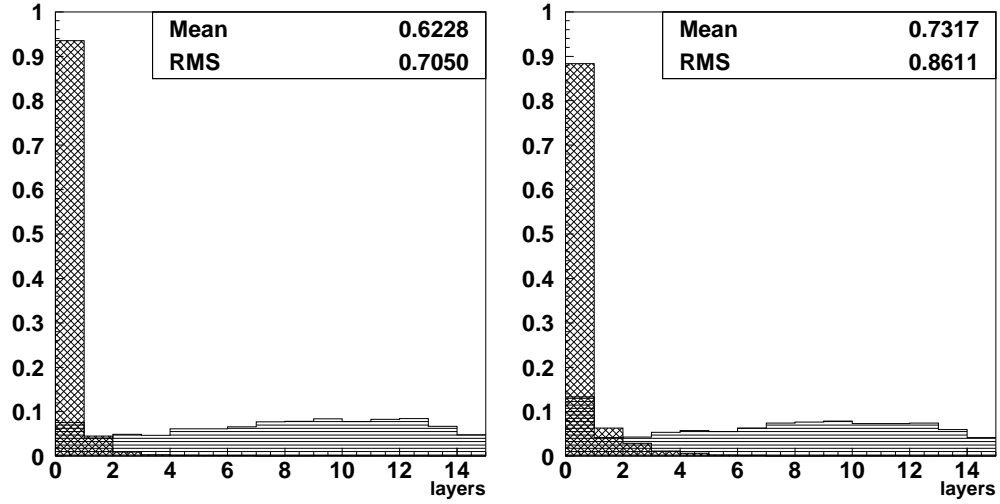
Figure 5.9: *The range difference distributions with Kalman filtering (left) and with blind extrapolation (right). In each plot, a crossed histogram is for muons and the histogram filled with horizontal lines is for pions. These values are measured at the outermost layer which had associated hits.*

	condition
momentum (GeV/c)	0.5-3.0
polar angle (degree)	20-150
azimuthal angle (degree)	0-360
the number of events	10000

Table 5.2: *Conditions of single track Monte Carlo simulation.*

41

Chapter 6

Performance

In this chapter, we present the performance of the muon identification program with Kalman filter. Efficiency and fake rate are investigated with both Monte Carlo simulation and real data taken with the BELLE detector in 1999. Finally the reconstruction of $J/\psi \rightarrow \mu\mu$ is demonstrated with real data.

6.1 Definition

Efficiency

Two types of efficiency are considered. One is the efficiency with respect to reconstructed tracks in the CDC, which is called "Global efficiency" in this study. Global efficiency is affected by many components of inner detectors, besides the shape of the KLM detector itself. To reduce this effect, it is effective to consider the efficiency with a correcction of the KLM acceptance. This is achieved by checking whether an extrapolated muon candidate can be sensed by RPC strips or not. It is defined as "Software efficiency". Their definitions are :

$$\text{Global efficiency} = \frac{N_\mu}{N_{\text{recon}}}, \tag{6.1}$$

where N_{recon} is the number of candidates reconstructed in the CDC and N_μ is the number of candidates identified as a muon, and

$$\text{Software efficiency} = \frac{N_\mu}{N_{\text{cand}}}, \tag{6.2}$$

where N_{cand} is the number of candidates successfully extrapolated to the KLM acceptance region.

Fake rate

Fake rate is, in other words, the efficiency of missidentifying pions (and K, e, p) as muons. Therefore the definition is almost the same as that of muon efficiency :

$$\text{Global fake rate} = \frac{N_{\text{cont}}}{N_{\text{recon}}}, \tag{6.3}$$

where N_{recon} is the number of candidates reconstructed in the CDC and N_{cont} is the number of candidates identified as a muon, and

$$\text{Software fake rate} = \frac{N_{\text{cont}}}{N_{\text{cand}}}, \tag{6.4}$$

where N_{cand} is the number of candidates successfully extrapolated to the KLM accenpance region.

6.2 Performance with Monte Carlo simulation

In this section, efficiency and fake rate with single track Monte Carlo simulation are shown. We compared the performance of Kalman filter with the optimized software for blind extrapolation [16].

6.2.1 Efficiency

Efficiency is evaluated as a function of momentum, polar angle, and azimuthal angle. The results are shown in Figure 6.1 and Figure 6.2.

Momentum dependence

Both cases show flat distribution, especially in high momentum region. Difference in lower momentum region is mainly due to the difference of the cut variables.

Polar angle dependence

Without Kalman filtering, the dip of efficiency is seen at the boundary region between barrel and endcap, forward and backward endcap region. Large resolution without Kalman filtering implies extrapolated candidate goes out of the KLM detector, and it can not be recovered any longer. In case of Kalman filtering, this effect becomes smaller, since the extrapolated track is close to the true muon track.
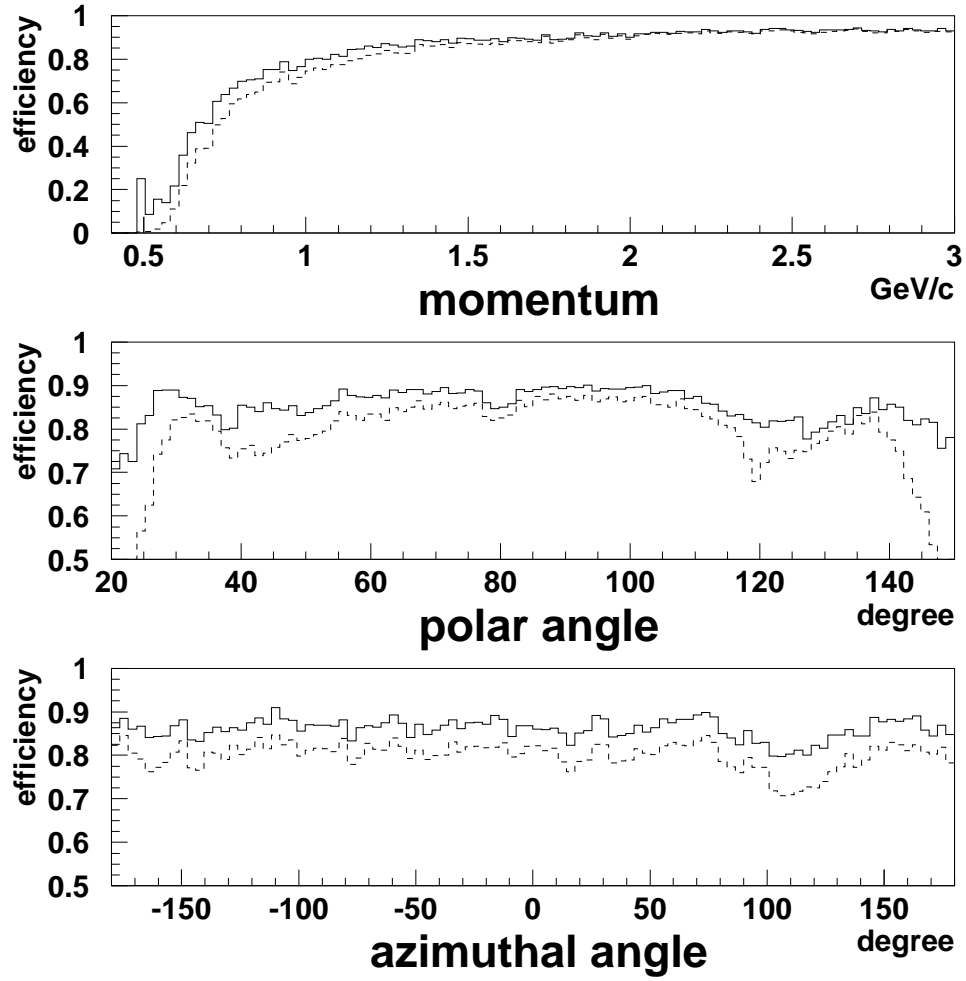
Figure 6.1: Muon identification efficiency with Kalman filter.
Solid lines are Software efficiency, and dashed lines are Global efficiency. All
the plots are made by single-track Monte Carlo simulation.
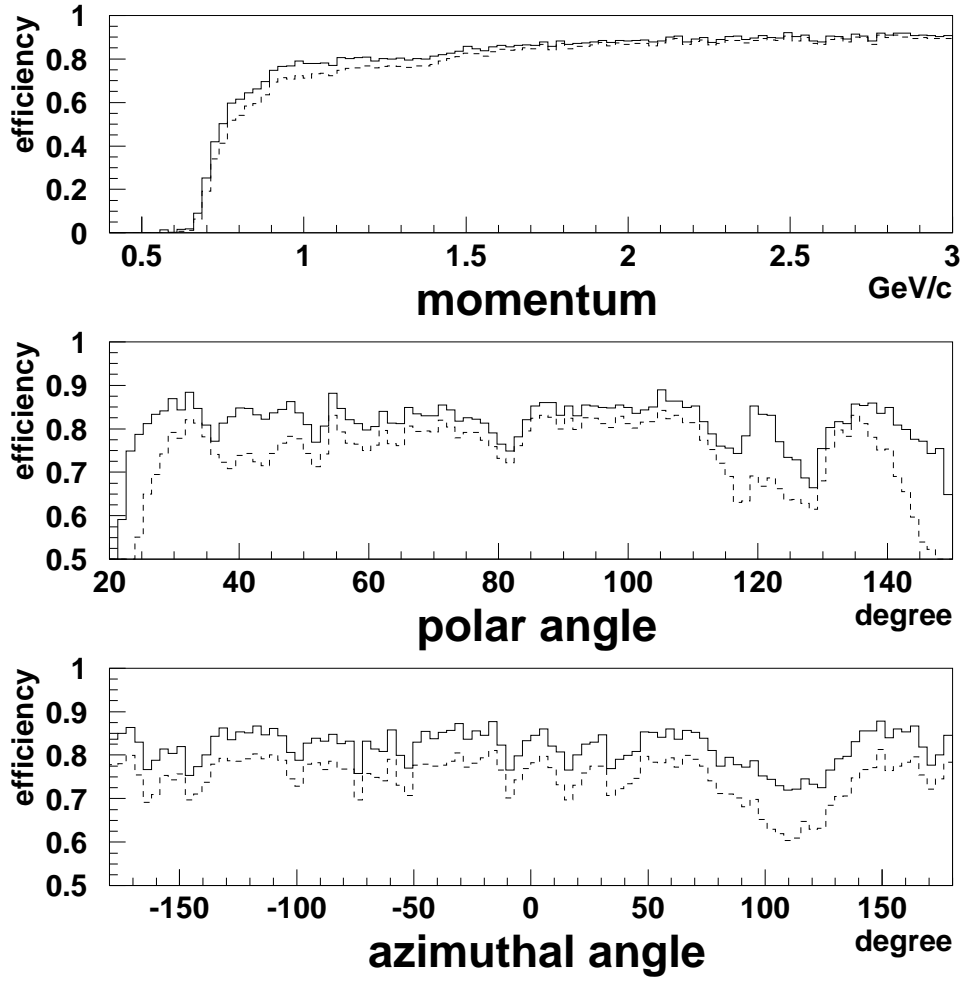
Figure 6.2: Muon identification efficiency without Kalman filter (blind extrapolation).
Solid lines are Software efficiency, and dashed lines are Global efficiency. Note that these plots were obtained by another muon identificaion tool which was served to KEK B-factory. All the plots are made by single-track Monte Carlo simulation.

Azimuthal angle dependence

Azimuthal angle dependence is almost flat, except around 90 degrees. It is due to "chimney" for the cryostat. Because the chimney penetrates the KLM, there is no RPC detector in this region. This naturally makes efficiency drop. Kalman filtering absorbs this effect.

6.2.2   Fake rate

The results are shown in Figure 6.3 and Figure 6.4.

Momentum dependence

With Kalman filter, averaged fake rate is lower than the case without Kalman filter in all the momentum regions. In very low momentum region, the fake rate becomes twice as that in the high momentum region without Kalman filter, but it is reduced with Kalman filter. Thus Kalman filter enlarges the accessible momentum region.

Angular dependence

Fake rate becomes flat with Kalman filter, both for polar angle and azimuthal angle distributions.
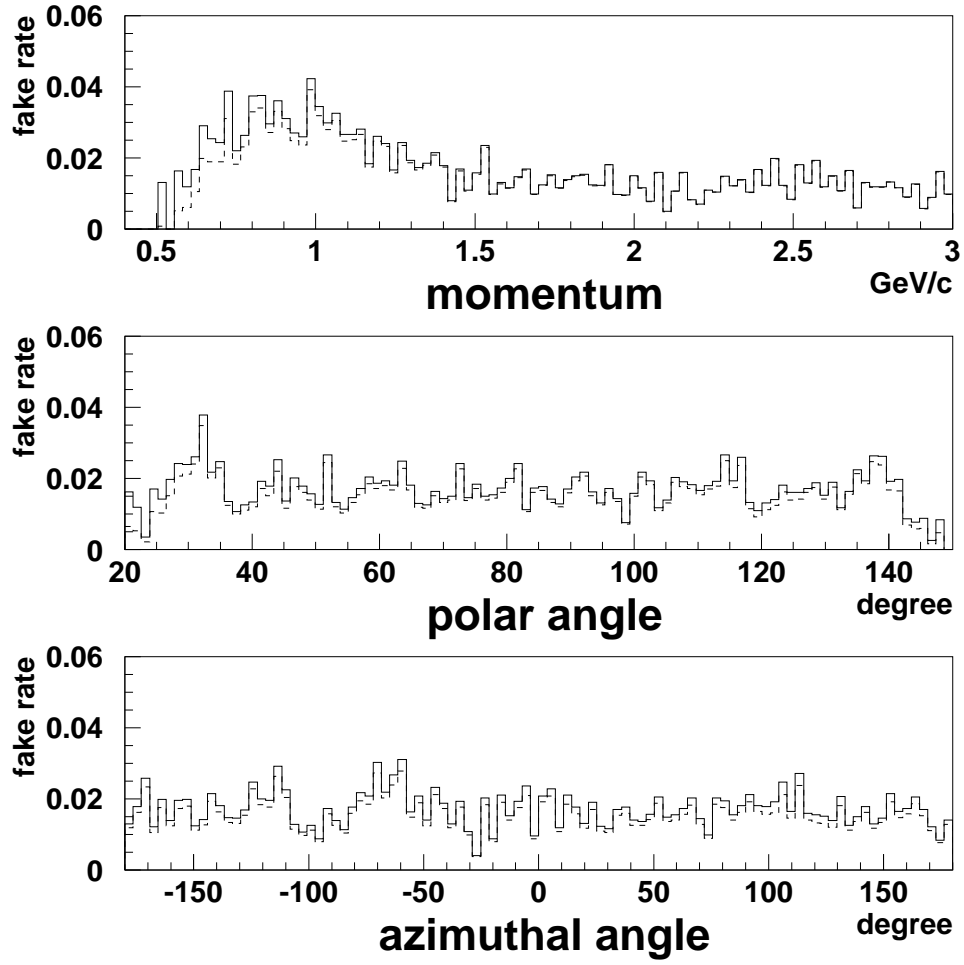
Figure 6.3: Pion fake rate with Kalman filter.
Solid lines are Software fake rate, and dashed lines are Global fake rate. All the plots are made by single-track Monte Carlo simulation.

47
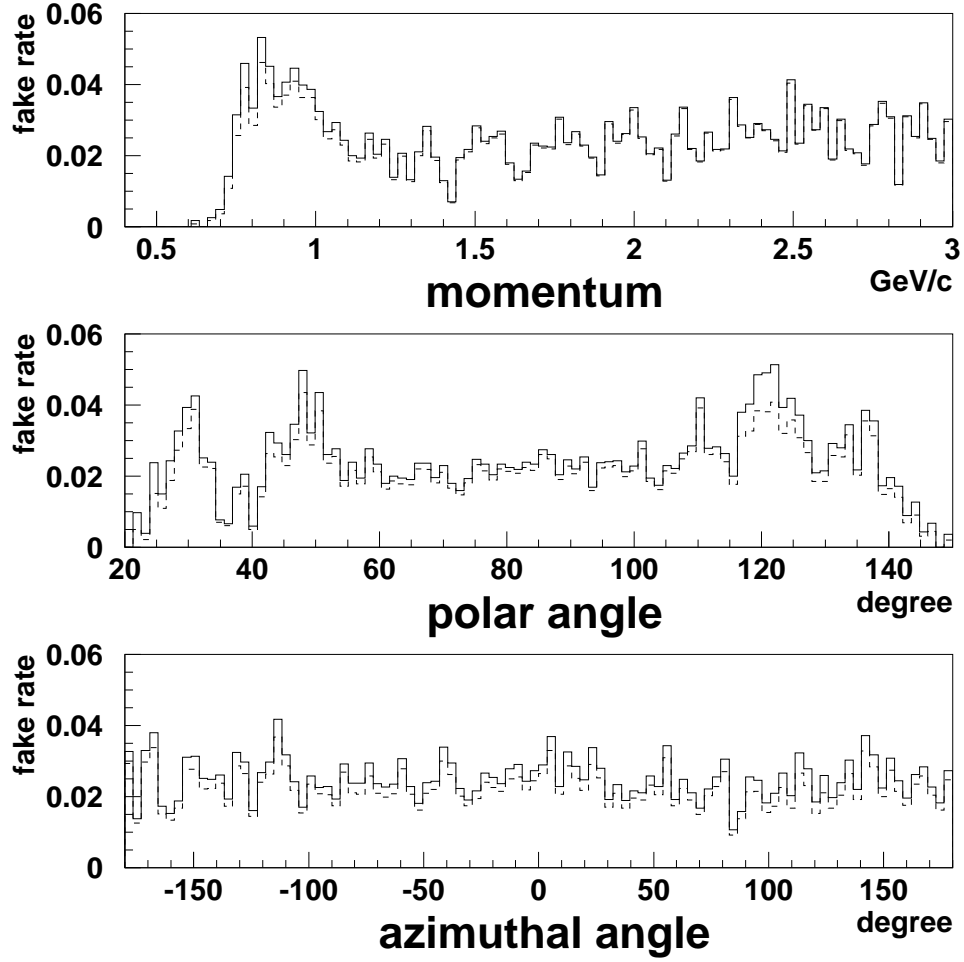
Figure 6.4: Pion fake rate without Kalman filter (blind extrapolation). Solid lines are Software fake rate, and dashed lines are Global fake rate. Note that these plots were obtained by another muon identificaion tool which was served to KEK B-factory. All the plots are made by single-track Monte Carlo simulation.

6.2.3 Classification of identified candidates

Figure 6.5 and Figure 6.6 show classification of identified muons and misidentified pions.

For muons, penetrating muons are obtained with high efficiency and muons decaying before the KLM are never identified. Though a small fraction of muon decaying in the KLM is lost, generally speaking the original distribution is kept in the whole momentum region. Almost all the scattered
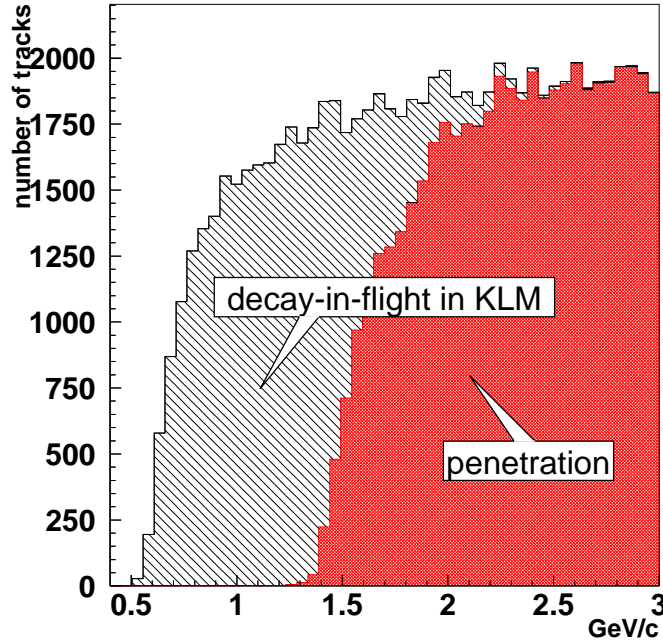
Figure 6.5: *Classification of identified prompt muons.*
This plot was made by Monte Carlo simulation with single muon track events.

pions are reduced in the whole mometum region. The largest component is pions decay-in-flight before the KLM detector. Distribution of such tracks is flat in mommentum, and shows the same behaviour as that of prompt muons. Furthremore, in high momentum region, penetrating pions share 20 % of the total fake rate. This particle is difficult to reject, because interaction is the same as prompt muons.

On the other hand, in lower momentum region, decay-in-flight pions in the KLM are the main source of contamination. This fact implies there may

be some room to improve muon identification performance, for example by detecting the point of decay-in-flight.
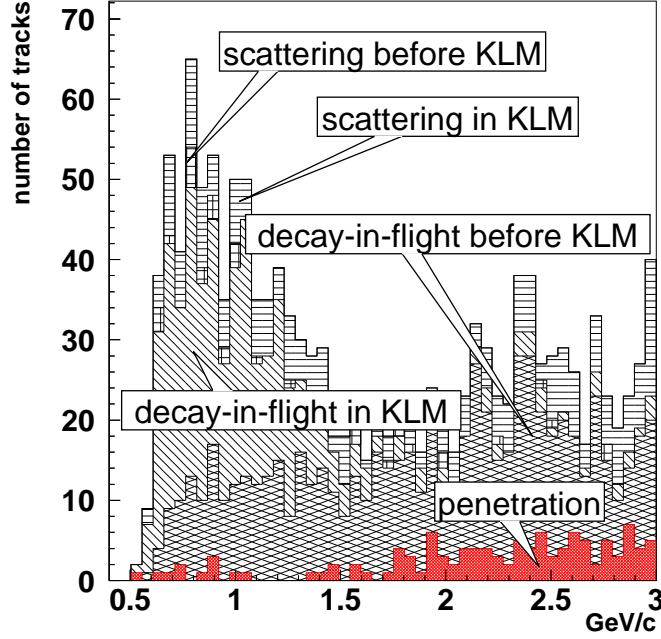
Figure 6.6: *Classification of misidentified prompt pions.*
This plot was made by Monte Carlo simulation with single pion track events.

6.3   Performance in Real Data

6.3.1   2 photon → $\mu\mu$

The 2 photon process is useful not only to study interesting physics (for example 2 photon → $\tau\tau$), but to study detector performance because of its wide momentum and polar angle ranges. Background events are also small. In this study, we use 2 photon → $\mu\mu$ mode to study muon identification performance. The Feynman diagram of this process is shown in Figure 6.7.

Selection criteria

The selection criteria are as follows :

- Pre-selection for 2 photon events [21]
    - $d_{Ri} < 5$ (cm)
    - $d_{Zi} < 5$ (cm)
    - $P_{Ti} > 0.3$ (GeV/c)
    - $17 < \theta_i < 150$ (degree)

- Cosmic ray reduction
    - $\theta_1 + \theta_2 < 174.75$ (degree)
    - $\theta_1 + \theta_2 > 185.63$ (degree)

- Beam background reduction
    - $-1.5 < d_{Z1} - d_{Z2} < 1.5$ (cm)
    - $-2.0 < d_{Z1} - d_{Z2} < 3.0$ (cm)

- Reduction of fake particles
    - Proton probability < 0.4
    - Electron probability < 0.4 or E/p< 0.8 or E/p> 1.2

- Event tagging
    - One of 2 tracks is used to confirm this event is really 2 photon $\mu\mu$ event (event tagging)
    - Another candidate is used to judge actual performance.

where $i = 1, 2$, P_{Ti} is the transverse momentum, θ_i is the polar angle of each candidate, d_{Zi} and d_{Ri} are impact parameter along beam direction and crossing direction, respectively.
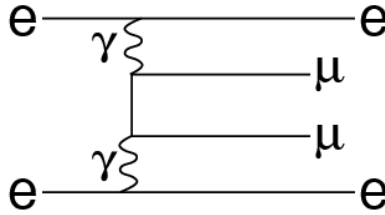
Figure 6.7: *2 photon $\to \mu\mu$ Feynman diagram.*
In many cases, electrons go down to the beam pipe and are unseen. There-fore only $\mu\mu$ are seen in the BELLE detector.

Performance

The efficiency is shown in Figure 6.8. The results with real data are consist with Monte Carlo simulation in the momentum region of interest. Consequently, it is ascertained that required momentum range to observe $J/\psi K_S$ event (See Figure 2.2) is covered with sufficient efficieny.
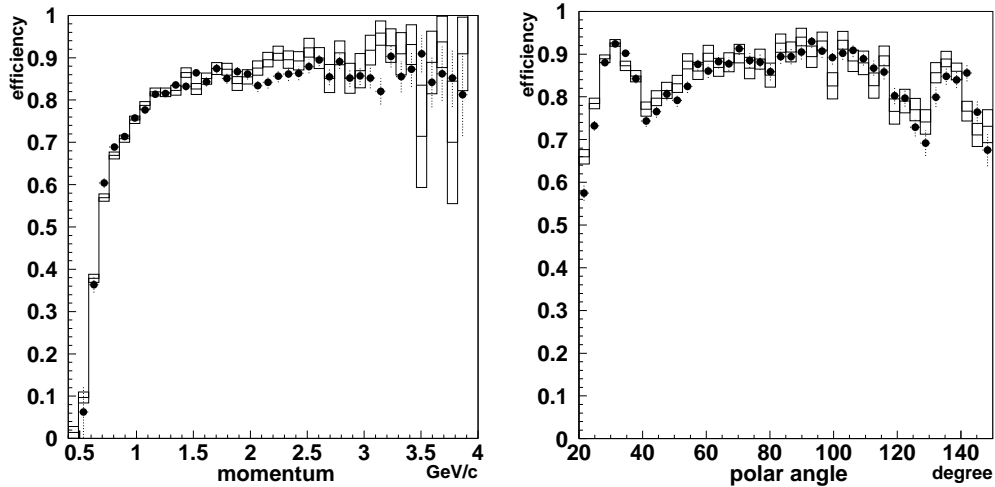
Figure 6.8: *2 photon $\rightarrow \mu\mu$ efficiency as a function of momentum (left) and polar angle (right). Black circles represent real data taken by BELLE 1999 runs. Open histograms are obtained by Monte Carlo simulation.*

6.3.2 Inclusive J/ψ

At last, we show the performance of muon identification with inclusive B decay to J/ψ ; i.e. $B \rightarrow J/\psi$X, where X means anything and J/ψ is reconstructed with $J/\psi \rightarrow \mu\mu$.

The selection criteria are as follows :

- Pre-selection to select events containing some hadronic tracks [21]

- Require two candidate tracks with an opposite charge.

- Require $P^* < 2$ (GeV/c) to reject J/ψ from continuum events, where P^* means the momentum of J/ψ candidate at $\Upsilon(4S)$ rest frame (kinematical cut).

- muon identification

- One candidate passes loose cut criteria.

- Another candidate passes usual cut criteria.

Figure 6.9 shows the dimuon invariant mass distribution. By estimating the number of background events with linear function, we estimated the number of reconstructed $J/\psi \to \mu\mu$ events :

$$N_{J/\psi \to \mu\mu} = 136 \pm 13 \text{ events,}\qquad(6.5)$$

where integrated luminosity is 239 pb^{-1} for the 1999 Autumn runs of KEK B-factory. This sharp peak clearly demonstrates that muon identification tool utilizing Kalman filter works as expected.
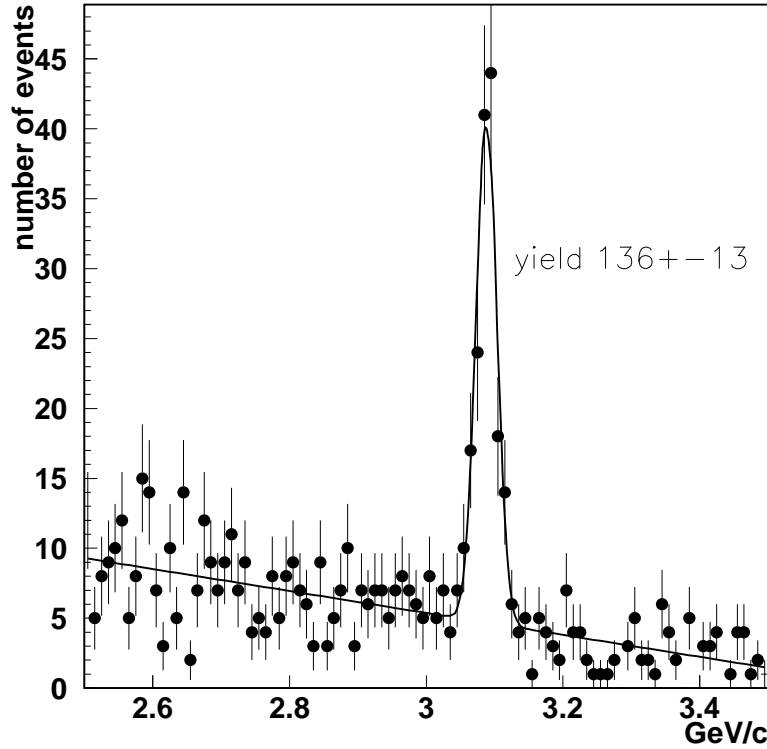
Figure 6.9: $J/\psi \to \mu\mu$ invariant mass distribution
Mass peak are seen around nominal mass of J/ψ (3096.88 $\pm$ 0.04 MeV) [19]. These J/ψ come from $B \to J/\psi$ X. Filled circle means data point. Each bin is seperated with 10 MeV/c width.

Criteria	# of events	Efficiency(%)	Total Efficiency(%)
$N_{J/\psi \to \mu\mu}$	10000		
Pre-selection	8992	89.9	89.9
Reconstruction	8086	89.9	80.9
Opposite charge	7737	95.7	77.4
Kinematical cut	7622	98.5	76.2
Muon identification	6049	79.4	60.5
Fitting	5935 ± 78	98.1 ± 1.8	59.3 ± 0.8

Table 6.1: *Results of event selection for $J/\psi \to \mu\mu$ Monte Carlo simulation.*

We can also estimate the branching ratio of $B \to J/\psi$X based on this result. First of all, $N_{J/\psi \to \mu\mu}$ is expressed as follows :

$$N_{J/\psi \to \mu\mu} = N_{B \to J/\psi\mathrm{X}} \times \mathbf{Br}(J/\psi \to \mu\mu) \times \varepsilon_{\mathrm{sel}} \times \varepsilon_{\mathrm{rec}} \times \varepsilon_{\mu\mathrm{ID}} \times \varepsilon_{\mathrm{fit}} \quad (6.6)$$

where $N_{B \to J/\psi\mathrm{X}}$ is the number of $B \to J/\psi$X events, $\mathbf{Br}(J/\psi \to \mu\mu)$ is the branching ratio of $J/\psi \to \mu\mu$ decays, $\varepsilon_{\mathrm{sel}}$ is the pre-selection efficiency, $\varepsilon_{\mathrm{rec}}$ is the reconstruction efficiency, $\varepsilon_{\mu\mathrm{ID}}$ is the muon identification efficiency and $\varepsilon_{\mathrm{fit}}$ is the fitting efficiency.

As $N_{J/\psi \to \mu\mu}$ is estimated and each efficiency can be estimated with Monte Carlo simulation, we can obtain $N_{B \to J/\psi\mathrm{X}}$. Table 6.1 shows Monte Carlo results of $B \to J/\psi\mathrm{X} \to \mu\mu$.

Since $\mathbf{Br}(J/\psi \to \mu\mu) = 6.01 \pm 0.19\%$ [19],

$$N_{B \to J/\psi\mathrm{X}} = 3843 \pm 400. \quad (6.7)$$

Since the number of produced $B^0 \bar{B}^0$ events is estimated to be 232420 [17],

$$
\begin{aligned}
N_{B \to \mathrm{anything}} \simeq 2 \times N_{B\bar{B}} &= 2 \times 232420 \\
&= 464840 \quad (6.8)
\end{aligned}
$$

Therefore, the branching ratio of $N_{B \to J/\psi\mathrm{X}}$ becomes

$$
\begin{aligned}
\mathbf{Br}(B \to J/\psi\mathrm{X}) &= \frac{N_{B \to J/\psi\mathrm{X}}}{N_{B \to \mathrm{anything}}} \\
&= 0.83 \pm 0.08(\%), \quad (6.9)
\end{aligned}
$$

where the error is statistical only. The result is not inconsistent with the previous experimental result of $1.12 \pm 0.04 \pm 0.06(\%)$ [18].

Chapter 7

Conclusion

CP violation is one of the hot topics of present elementary particle physics. The KEK B-factory is one of facilities to study it with producing a large number of B mesons. Identification of muons at the KEK B-factory is important as the most promising decay mode of B meson is $B \to J/\psi K_S$ where J/ψ further decays into $\mu^+\mu^-$ and e^+e^- .

For identification of muons, its character was compared with other charged particles which are pions, kaons, electrons and protons. Since muons are able to penetrate a large amount of material, a measurement of range is effective. Though a small fraction of pion penetrates such material also, they can be rejected by calculating χ^2's for associated hits. In order to take the scattering effect into account, methods with progressive fit are preferred for the precise estimation of χ^2 . Therefore simultaneous measurements of range and χ^2 are needed to identify muons.

In order to meet this requirement, we developed muon identification software adopting Kalman filter algorithm which is one of the most popular tools to realize progressive fitting Although the Kalman filter has been used for track fitting, in several experiments it has not been widely used to identify muons in spite of its potential advantages.

Muon identification efficiency and pion fake rate were estimated with Monte Carlo simulation. Both results showed sufficient performance to identify muons and reject pions at the same time.

The performance was also investigated with the data taken at the KEK B-factory in Autumn 1999. We looked at the two photon $\to \mu\mu$ process to evaluate the identification efficiency, and obtained good agreement between the real and Monte Carlo data in the momentum range enough to cover muons from $J/\psi K_S$ events. In the end, we demonstrated the reconstruction

of inclusive B decays into J/ψ ($\to \mu^+\mu^-$). From the signal yield of (136 ± 13) events collected with an integrated luminosity of 239 pb^{-1}, the branching fraction was estimated to be $\mathbf{Br}(B \to J/\psi\mathrm{X}) = 0.83 \pm 0.08(\%)$.

With these results, we conclude that muon identification with the Kalman filter algorithm satisfies the requirements at the KEK B-factory and will play an essential role in measuring the $\mathbf{CP}$ asymmetry in B decays.

Appendix A

CP violation

A.1 C,P,T symmetry

Historically speaking, various conservation laws are discovered by many physicists. Nowadays, it is widely known that each conservation laws are related to the symmetry of our universe. In quantum theory, several conservation laws which are corresponding to discrete transformations, are known.

Charge transformation Charge transformation **C** is the operation to exchange the particle for the anti-particle. We can't say which is original or exchanged one, since both following the same physical law.

Parity transformation Parity transformation **P** is the operation to project one vector to "mirror". The vectors like spatial vector $\vec{r}$ and momentum vector $\vec{p}$ change their own sign (parity-), but some producted vector like the angular momentum $\vec{L} = \vec{r} \times \vec{p}$ don't change (parity +).
Anyway, original vector and projected one seem following the same physical law. It means we can't distinguish our universe and the universe in the mirror.

Time transformation Time transformation **T** is the operation to reverse the flow of time. For example, momentum vector $\vec{p}$ change its sign, but still follow same physics law. This transformation can't be distinguished original and reversed one also.

And more, the project of the above three transformation **CPT** are invariant for local interaction. It is guaranteed by **CPT** theorem, and no experimental evidence are seen to break it. Of course, it has been considered

that each transformation about $\mathbf{C}, \mathbf{P}, \mathbf{T}$ are invariant for any interactions ,also. The world was symmetric.

A.2   C and P violation

In 1957, the violation of $\mathbf{C}$ and $\mathbf{P}$ in weak interaction were founded in the β decay of ^{60}Co by C.S.Wu, based on the suggestion of Lee and Yang. However, it seemed that their product, $\mathbf{CP}$ was still invariant.

A.3   CP violation at K decay

$\mathbf{CP}$ violation at neutral K meson system was predicted by Gell-Mann and Paris.

There are two neutral K mesons, K^0 and $\bar{K}^0$, where K^0 consists of $\bar{s}$ and d quark ($S = +1$). Other hand, $\bar{K}^0$ consists of s and $\bar{d}$ quark ($S = -1$). In fact, both mesons are not $\mathbf{CP}$ eigenstates, but mass eigenstates. So, we rewrite them to $\mathbf{CP}$ eigenstates with following formula :

$$|K_1\rangle = \frac{|K^0\rangle + |\bar{K}^0\rangle}{\sqrt{2}} \tag{A.1}$$

$$|K_2\rangle = \frac{|K^0\rangle - |\bar{K}^0\rangle}{\sqrt{2}} \tag{A.2}$$

They satisfy :

$$\mathbf{CP}|K_1\rangle = +|K_1\rangle \tag{A.3}$$

$$\mathbf{CP}|K_2\rangle = -|K_2\rangle \tag{A.4}$$

Experimentally, two neutral K mesons are observed : short lived K_{S} and long lived K_{L}. K_{S} mainly decays into two π, $\pi^+\pi^-$ or $\pi^0\pi^0$, and K_{L} has decay mode to three π mode, $\pi^+\pi^-\pi^0$ or $\pi^0\pi^0\pi^0$ and semi-leptonic mode, $\pi^\pm\mu^\mp\nu(K^0_{\mu 3})$ or $\pi^\pm e^\mp\nu(K^0_{e3})$, and so on. Well, consider about $\mathbf{CP}$ phase of two π and three π. $\mathbf{CP}(\pi^+\pi^-) = +\mathbf{1}$ for ground state of this two-body system, since π is boson, both π are symmetric to exchange, so $\mathbf{CP}(\pi^+\pi^-) \overset{\mathbf{C}}{\to} \mathbf{CP}(\pi^-\pi^+) \overset{\mathbf{P}}{\to} \mathbf{CP}(\pi^+\pi^-)$. Otherhand, $\mathbf{C}(\pi^\mathbf{0}) = +\mathbf{1}$ for $\mathbf{C}(\pi^\mathbf{0})$ decays to two γ, where $\mathbf{C}(\gamma) = -\mathbf{1}$. It means $\mathbf{CP}(\pi^+\pi^-\pi^\mathbf{0}) = -\mathbf{1}$. Therefore, the decay into $\pi^+\pi^-$ is allowed for the K_1, but forbidden for the K_2 if $\mathbf{CP}$ are conserved. This $\mathbf{CP}$ study suggests $K_S = K_1$, $K_L = K_2$, because it is considered as explanation why long lived K_{L} has really longer life than K_{S}.

However, in 1964, Christenson, Cronin, Fitch and Turlay discovered that the long lived K_L also decays into $\pi^+\pi^-$ with a branching ratio of $\sim 2\times10^{-3}$. This decay mode obviously say the existence of **CP** violation. Both K_S and K_L are no longer the **CP** eigen states :

$$\mathbf{CP}|K_S\rangle = \frac{1}{\sqrt{1+|\varepsilon|^2}}(\mathbf{CP}|K_1\rangle + \varepsilon\mathbf{CP}|K_2\rangle), \tag{A.5}$$

$$\mathbf{CP}|K_L\rangle = \frac{1}{\sqrt{1+|\varepsilon|^2}}(\mathbf{CP}|K_2\rangle + \varepsilon\mathbf{CP}|K_1\rangle), \tag{A.6}$$

where ε is a complex number.

A.4 CP violation in the Standard Model

In the Standard Model with SU(2) × SU(1) as the gauge group of electroweak interactions, both the quarks and leptons are assigned to be left-handed doubblets and right-handed singlets. Especially for three generations quarks, their charged current J^μ are given by :

$$J^\mu = (\bar{u}\ \ \bar{c}\ \ \bar{t})\frac{\gamma^\mu(1-\gamma^5)}{2}V\begin{pmatrix} d \\ s \\ b \end{pmatrix}, \tag{A.7}$$

where V is the 3×3 complex mixing matrix ,called as the Cabbibo-Kobayashi-Maskawa matrix (CKM matrix).

$$
\begin{aligned}
V &= \begin{pmatrix} V_{ud} & V_{us} & V_{ub} \\ V_{cd} & V_{cs} & V_{cb} \\ V_{td} & V_{ts} & V_{tb} \end{pmatrix} \\
&= \begin{pmatrix} c_1 & -s_1c_3 & -s_1s_3 \\ s_1c_2 & c_1c_2c_3 - s_2s_3e^{i\delta} & c_1c_2s_3 - s_2c_3e^{i\delta} \\ s_1s_2 & c_1s_2c_3 + c_2s_3e^{i\delta} & c_1s_2s_3 - c_2c_3e^{i\delta} \end{pmatrix},
\end{aligned} \tag{A.8}
$$

where $c_i = \cos\theta_i, s_i = \sin\theta_i, \theta_i (i = 1, 2, 3)$ is the mixing angles and δ is the observable phase. In fact, more than three generations only allow to exist of such phase, give **CP** and **T** violation in the Standard Model.

Wolfenstein described V to very convenient approximate formula using four parameters :

$$V \cong \begin{pmatrix} 1 - (\lambda^2/2) & \lambda & A\lambda^3(\rho - i\eta) \\ -\lambda & 1 - (\lambda^2/2) & A\lambda^2 \\ A\lambda^3(1 - \rho - i\eta) & -A\lambda^2 & 1 \end{pmatrix}, \tag{A.9}$$

where $\lambda = \sin\theta_c, \theta_c \sim 0.22$ is the Cabbibo angle, well determined by strange particle decays, nuclear β decay, the production of charm in ν interaction, and so on. A is determined from $|V_{cb}|$, obtained from measurement of semi-leptonic decays of B meson and from B meson life time τ_B. The relative strength of $b \to u$ and $b \to c$ transition in semi-leptonic B decays can determine $\sqrt{\rho^2 + \eta^2}$.

The requirement of unitarity to V lead one interesting relation :

$$V_{ud}V_{ub}^* + V_{cd}V_{cb}^* + V_{td}V_{tb}^* = 0, \qquad (A.10)$$

This is the unitarity triangle what we call, a closed triangle on the complex plane. The form of this triangle is shown in Figure A.1.
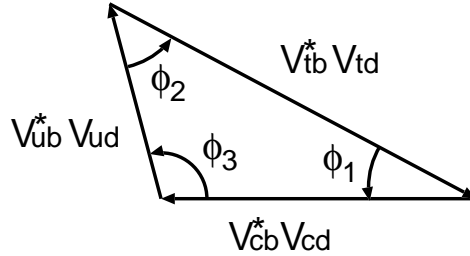
Figure A.1: *The unitarity triangle of the CKM matrix*

The three internal angles of the triangle are defined as

$$\phi_1 = \pi - arg\left(-\frac{V_{tb}^*V_{td}}{-V_{cb}^*V_{cd}}\right), \qquad (A.11)$$

$$\phi_2 = arg\left(\frac{V_{tb}^*V_{td}}{-V_{ub}^*V_{ud}^*}\right), \qquad (A.12)$$

$$\phi_3 = arg\left(\frac{V_{ub}^*V_{ud}}{-V_{cb}^*V_{cd}}\right). \qquad (A.13)$$

To proof KM thorem, precise measurement of above three side and three angle of unitarity triangle.

A.5 CP violation at B physics

CP violation at B meson are classified to several types : direct **CP** violation, indirect **CP** violation and indirect **CP** violation in decays of mixed $B^0\bar{B}^0$. These difference are correspond to different mechanism for violation.

A.5.1 CP violation in decay of B

Direct **CP** violation means different decay width between B and $\bar{B}$:

$$\Gamma(B \to f) \neq \Gamma(\bar{B} \to \bar{f}) \tag{A.14}$$

It occurs through the interference of more than one diagrams which have different phases. For example, there are two leading diagram, tree and penguin (Figure A.2).

Usual process is tree, and penguin contribution can be negligible. But some process like $B^0 \to \pi^+ \pi^-$ mode which is a measurement mode of ϕ_2 , penguin contribution may not be neglected.
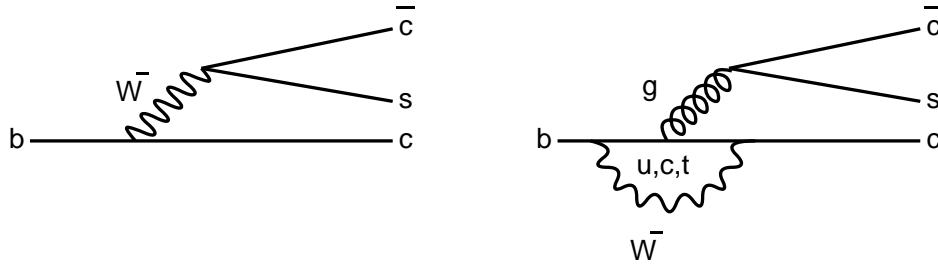
Figure A.2: *left:Tree diagram right:Penguin diagram.*

A.5.2 CP violation in $B^0 \bar{B}^0$ mixing

Generally, the Hamiltonian of the particle which decay is :

$$\hat{H} = \hat{M} - \frac{i}{2}\hat{\Gamma}, \tag{A.15}$$

where $\hat{M}$ is mass operator, real part of $\hat{H}$, $\hat{\Gamma}$ is decay operator, imaginary part of $\hat{H}$.

The flavor status B^0 and $\bar{B}^0$ are eigenstates of the strong and electromagnetic interactions, but not weak interaction, which is responsible for their decay. So, we can expect there is mixing between both flavor similar to neutral K system. In mass eigenstates, there are two neutral B mesons, lighter B_L which has mass m_L and width Γ_L, and heavier B_H which has mass m_H and width Γ_H :

$$
\begin{aligned}
|B_L\rangle &= p|B^0\rangle + q|\bar{B}^0\rangle, \tag{A.16}\\
|B_H\rangle &= p|B^0\rangle - q|\bar{B}^0\rangle \tag{A.17}
\end{aligned}
$$

Their Hamiltonian are :

$$\mathcal{H} = \begin{pmatrix} M_{11} & M_{12} \\ M_{21} & M_{22} \end{pmatrix} - \frac{i}{2} \begin{pmatrix} \Gamma_{11} & \Gamma_{12} \\ \Gamma_{21} & \Gamma_{22} \end{pmatrix}. \qquad (A.18)$$

CPT invariance implies that the diagonal components of $\mathcal{H}$ are equal :

$$\mathcal{H} = \begin{pmatrix} M & M_{12} \\ M_{12}^* & M \end{pmatrix} - \frac{i}{2} \begin{pmatrix} \Gamma & \Gamma_{12} \\ \Gamma_{12}^* & \Gamma \end{pmatrix}. \qquad (A.19)$$

In this term, p and q become :

$$\frac{q}{p} = \frac{1 - \varepsilon_B}{1 + \varepsilon_B} = \sqrt{\frac{M_{12}^* - (i/2)\Gamma_{12}^*}{M_{12} - (i/2)\Gamma_{12}}} \qquad (A.20)$$

If ε_B is non-zero, it indicates indirect **CP** violation in B^0-$\bar{B}^0$ mixing from its definition. It is same mechanism as indirect **CP** violation at neutral K. However, much larger mass of B ($\Gamma_{12} \ll M_{12}$) compared by K ($\Gamma_{12} \sim 2M_{12}$) makes ε_B too small to be observed.

A.5.3 CP violation in decays of mixed $B^0 \bar{B}^0$

The most hopeful scenario to be observed **CP** violation in neutral B system are that both B^0 and $\bar{B}^0$ decay into same **CP** eigenstate final state $f_{\mathbf{CP}}$.

$$A = \langle f_{\mathbf{CP}} | \mathcal{H} | B^0 \rangle, \qquad (A.21)$$
$$\bar{A} = \langle f_{\mathbf{CP}} | \mathcal{H} | \bar{B}^0 \rangle, \qquad (A.22)$$
$$\qquad (A.23)$$

Here, define useful value :

$$\lambda = \frac{q}{p} \cdot \frac{\bar{A}}{A} \qquad (A.24)$$

and mixing. To know what this producted value really means, consider about following **CP** asymmetric parameter $a_{f_{\mathbf{CP}}}$:

$$a_{f_{\mathbf{CP}}}(\Delta t) = \frac{\Gamma(\bar{B}^0(\Delta t) \to f_{\mathbf{CP}}) - \Gamma(B^0(\Delta t) \to f_{\mathbf{CP}})}{\Gamma(\bar{B}^0(\Delta t) \to f_{\mathbf{CP}}) + \Gamma(B^0(\Delta t) \to f_{\mathbf{CP}})} \qquad (A.25)$$

$$= \frac{|\lambda_{f_{\mathbf{CP}}}|^2 - 1}{|\lambda_{f_{\mathbf{CP}}}|^2 + 1} \cos \Delta M \Delta t + \frac{2 Im(\lambda_{f_{\mathbf{CP}}})}{|\lambda_{f_{\mathbf{CP}}}|^2 + 1} \sin \Delta M \Delta t \quad (A.26)$$

where $\Delta M = M_{B_H} - M_{B_L}$, $\Delta t = t_{\mathbf{CP}} - t_{\mathbf{TAG}}$, $t_{\mathbf{CP}}$ is the decay time for the side which decays into **CP** eigenstate, and $t_{\mathbf{TAG}}$ is the decay time for

opposite side used by tagging flavor of B^0 meson. Well, even if there is no **CP** violation both direct ($\bar{A}_{\textbf{CP}}/A_{\textbf{CP}} = 1$) and indirect ($q/p \sim 1$),

$$
\begin{aligned}
a_{f_{\textbf{CP}}}(\Delta t) &= Im(\lambda_{f_{\textbf{CP}}})\sin\Delta M\Delta t & \text{(A.27)} \\
&= \pm\sin 2(\phi_M + \phi_D)\sin\Delta M\Delta t, & \text{(A.28)}
\end{aligned}
$$

where ϕ_M is the phase related q/p, ϕ_D is the phase related decay into $f_{\textbf{CP}}$.

This type of **CP** violation is so useful for B physics. For example, $B^0 \to J/\psi K_S$:

$$
\begin{aligned}
\lambda(J/\psi K_S) &= \left(\frac{q}{p}\right)_B \left(\frac{\bar{A}_{J/\psi K_S}}{A_{J/\psi K_S}}\right) \left(\frac{q}{p}\right)_K & \text{(A.29)} \\
&= -\left(\frac{V_{tb}^* V_{td}}{V_{tb} V_{td}^*}\right) \left(\frac{V_{cs}^* V_{cb}}{V_{cs} V_{cb}^*}\right) \left(\frac{V_{cd}^* V_{cs}}{V_{cd} V_{cs}^*}\right) & \text{(A.30)}
\end{aligned}
$$

$$
a_{f_{\textbf{CP}}}(\Delta t) = \sin 2\phi_1 \sin \Delta M\Delta t \qquad \text{(A.31)}
$$

In short, this decay mode is sensitive to ϕ_1, one angle of unitarity triangle and to be determined by decay time measurement of both side. This Feynman diagram is shown in Figure 2.1.

Appendix B

KEK B-Factory

B.1   BELLE detector

B.1.1   Silicon Vertex Detector (SVD)

As described former section, the main purpose of BELLE experiment is to observe time-dependent **CP** assymetry in $B^0\bar{B}^0$ decays. The SVD is charged to reconstruct the decay vertex of each B meson in order to determine the time difference between two Bs.

Since B meson has $200\mu m$ decay length (distance between the KEKB interaction point and its decay point) in average, the required resolution for vertex reconstruction is in the order of $100\mu m$. Furthermore, to avoid the influence of multiple Coulomb scattering, the amount of material of the SVD must be minimized.

Double-sided Silicon Strip Detector (DSSD) was adopted as the detector satisfying such harsh requirement. Three layers of double-sided 300 μm-thick silicon strip sensor boards, spanning from 3.0 to 6.05 cm in r-phi. For each layer, p-sides are used for ϕ readouts with 50 μmpitch and n-sides are used for z readouts with 84 μmpitch. Number of readout channels is 81,920.

B.1.2   Central Drift Chamber (CDC)

Central Drift Chamber (CDC) has two important role. One is to reconstruct charged tracks for measurement momentum of the track from its curvature, the other is to measure energy loss (dE/dx) inner the CDC, which is not dependent on the kind of particle, but dependent on the velocity ($\beta = v/c$). So, the kind of particles are specified with both information.

The CDC looks like a cylinder which inner and outer radii are respectively 8 and 88 cm, filled by 50 sense wire layers and 3 cathode strip layers. The sense-wire layers are grouped into 11 super layers : 6 axial and 5 stereo super layers. Stereo angles range from 42.5 mr to 72.1 mr. The number of readout channels is 8,400 for anode wires and 1,792 for cathode strips. A 50% helium-50% ethane gas mixture is used in the chamber to minimize the multiple Coulomb scattering contribution to the momentum resolution.

B.1.3 Aerogel Čherenkov Counter (ACC)

The ACC is the threshold Čherenkov Counter system consists of silica aerogel radiators. Čherenkov radiation is the phenomenon occurring in the matter caused by passing of the charged track : assume the material is indexed by refractive $= n$. when the momentum of the charged particle in the matter exceeds

$$n > 1/\beta = \sqrt{1 + (m/p)^2}$$

the matter radiates Čherenkov light.

So, π and K are discretely separated by adjusting the threshold : π exceeds but K doesn't. It takes one part of π/K separation which is high momentum region above 1.2 GeV/c, on itself.

Each ACC module consists of fine-mesh photo multiplier tubes to detect Čherenkov radiation. The typical aerogel module comprises aerogel tiles contained in a 0.2-mm-thick aluminum box. The inner surface of the box is lined with Goretex sheet as the reflector. The barrel part of the ACC consists of 960 aerogel counters; 16-fold segmentation in z and 60-fold segmentation in ϕ. Five different indices of reflection, n = 1.01, 1.013, 1.015, 1.020 and 1.028, are used depending on polar angle θ (angle with respect to the beam axis). Each barrel counter is viewed by one or two fine-mesh photo-multipliers (FM-PMT's). The endcap part of the ACC has 228 counters in total with n = 1.03 and is structured in five concentric rings with 36-, 36-, 48-, 48-, and 60-fold segmentation from inside to outside. Each endcap counter is viewed by one FM-PMT through an air light guide. The number of readout channels is 1,560 in the barrel and 228 in the endcap.

B.1.4 Time of Flight counter (TOF)

The Time of Flight (TOF) using plastic scintillation counter is a very powerful method for particle identification. It is required to have a 100ps time resolution in order to provide 3σ π/K separation for momentum below 1.2GeV/c.

One 5-mm-thick Trigger Scintillation Counter (TSC) layer and two 4-cm-thick Time-of-Flight counter (TOF) layer separated by a 2-cm gap are located at r = 120 cm. The TOF is segmented into 128 in ϕ sectors and readout by one FM-PMT at each end. TSC's have 64-fold segmentation and are readout from only backward end by a single FM-PMT. The number of readout channels is 256 for the TOF and 64 for TSC.

B.1.5   Cesium Iodide Calorimeter (ECL)

The target particles of electro-magnetic calorimeter (ECL) are photons and electrons which make electro-magnetic shower inner the ECL cluster. The ECL detect that showers, and measure its energy.

Since there are a plenty of π^0 of B meson daughters and π^0 decays into 2 γ, detection of photon with high efficiency and energy resolution is an important issue, especially for low energy photon. π^0 mass resolution is dominated by the photon energy resolution. Sensitivity to and resolution of low energy photons are the critical parameters for the efficient π^0 detection.

Electron identification in BELLE relies primarily on a comparison of the charged particle track momentum and the energy it deposits in the electro-magnetic calorimeter. Good energy resolution of the calorimeter results in better hadron rejection.

In order to satisfy these requirements, we chose a design of the electro-magnetic calorimeter based on CsI (Tl) crystal. All CsI (Tl) crystals are 30cm (16.1 radiation length) long, and are assembled into a tower structure pointing near the interaction point. The barrel part of the ECL has 46-fold segmentation in θ and 144-fold segmentation in ϕ.

The forward (backward) endcap part of the ECL has 13-(10-) fold segmentation in θ and the ϕ segmentation varies from 48 to 144 (64 to 144). The barrel part has 6,624 crystals and the forward (backward) endcap part has 1,152 (960) crystals. Each crystal is readout by two 10mm×20mm photodiodes. Total readout channel is 17,472. The inner radius of the barrel part is 125cm. The forward (backward) endcap part starts at z=+196cm (-102cm).

Several tests were performed with a photon beam provided from the backward Compton scattering between electrons and laser photon

B.1.6 K_L and Muon Detector (KLM)

The K_L and Muon Detector (KLM) is designed to detect neutral kaons which cannot be identified by inside PID detectors and muons which penetrate

almost all detectors.

The KLM detector consists of a barrel part and two endcap parts. Fourteen layers of 4.7 cm thick iron plate and each Resistive Plate Counter (RPC) superlayer contains two RPC planes and provides θ and ϕ information. The barrel part has one additional RPC superlayer in front of the first iron plate. RPC is made of 2-mm thick glass electrodes. The iron plate is an absorber material for the KLM and also serves as the return path of magnetic flux provided by solenoid magnet. Nominally, the detector covers the polar angle range of $25° \leq \theta \leq 145°$. Signals are readout by ≈ 5 cm wide cathode strips in both θ and ϕ. The number of readout channels is 21,856 in barrel and 16,128 in endcap.

A detailed description of the KLM was already described.

Table B.1: *Performance parameters of the BELLE detector.*

Detector	Type	Configuration	Readout	Performance
Beam pipe	Beryllium double-wall	Cylindrical, r=2.3 cm 0.5mm Be/2mm He /0.5mm Be		Helium gas cooled
SVD	Double Sided Si Strip	300 μm-thick, 3 layers r = 3.0 - 5.8 cm Length = 22 - 34 cm	81.9 K	$\sigma_{\Delta z} \sim 105$ μm
CDC	Small Cell Drift Chamber	Anode: 52 layers Cathode: 3 layers r = 8.5 - 90 cm -77$\leq z \leq$ 160 cm	A: 8.4 K C: 1.5 K	$\sigma_{r\phi} = 130$ μm $\sigma_z = 200 \sim 1,400 \mu$m $\sigma_{p_t}/p_t = 0.3\%\sqrt{p_t^2+1}$ $\sigma_{dE/dx} = 6\%$
ACC	$n : 1.01 \sim 1.03$ Silica Aerogel	$\sim$12x12x12 cm^3 blocks 960 barrel / 228 endcap FM-PMT readout	1,788	$\mu_{eff} \geq 6$ K/π 1.2<p<3.5GeV/c
TOF	Scintillator	128 ϕ segmentation r = 120 cm, 3 m-long	128$\times$2	$\sigma_t = 100$ ps K/π up to 1.2GeV/c
ECL	CsI	Towered structure $\sim$ 5.5x5.5x30 cm^3 crystals Barrel: r = 125 - 162 cm Endcap: z = -102 and +196 cm	6,624 1,152(f) 960(b)	$\sigma_E/E=$ 0.67%/$\sqrt{E}\oplus$1.8% σ_{pos}=0.5 cm/$\sqrt{E}$ E in GeV
MAGNET	super conducting	inn.rad. = 170 cm		B = 1.5 T
KLM	Resistive Plate c.	14layers (5cm Fe+4cm gap) two RPCs in each gap θ and ϕ strips	θ:16 K ϕ:16 K	$\Delta\phi=\Delta\theta$=30mr for K_L σ_t=1ns 1% hadron fakes

B.2 Particle Identification

At BELLE and KEKB condition, some particles which are γ, $e^{\pm}$, $\mu^{\pm}$, $\pi^{\pm}$, $K^{\pm}$, K_L, etc. can be detected as "stable", the others are reconstructed from these "stable" particles. So, it is very important issue to detect effectively and identify correctly such particles. Some particles are identified by one sub-detector, the others are identified with combined information taken by a few sub-detectors.

B.2.1 dE/dx information

The CDC is used.
Because of 1.5 T magnetic field in the CDC, charged particles are strongly drifted and draw long traject. It allows the CDC to measure the momentum and dE/dx, the deposit energy per unit length. Since it is known that dE/dx is the function of the velocity, and this shape of function is different of the each particle kind, particle identification can be done in the CDC.

B.2.2 γ identification

The CDC and the ECL are used.
Since γ is one of neutral particle, it doesn't make any track at the CDC, but make cluster hit at the ECL due to electro-magnetic shower.

In short, the required condition for γ identification is the existence of hitted cluster in the ECL and no matching with any charged track extrapolated from the CDC.

B.2.3 e/π separation

The CDC and the ECL are used.
Even if same momentum is measured between electron and charged π, the big difference is seen at the ECL. At the ECL, electron deposits much larger energy at the ECL, because of electro-magnetic shower. This feaure is indexed by E/p, the ratio of measured energy deposit at the ECL and measured momentum at the CDC, hence electron and charged π can be separated.

B.2.4 π/K separation

The CDC, TOF and ACC are used.
Though charged K and π have almost same character, the mass of K is 5

times larger than π. Since momentum of charged particle is always measured by the CDC, it is needed the velocity to know the mass.

If measured momentum is lower than 1.2 GeV/c, it is available the velocity measured by the TOF. But if momentum exceeds 1.2 GeV/c, velocity measurement become difficult. The ACC is adjusted to work at such high momentum range. If the velocity is higher than the threshold decided at the ACC, Čherenkov radiation is emmited and measured. So, K and π are discretely separated.

B.2.5 μ identification

The CDC and the KLM are used.
Precise method for muon identification is already mentioned.

B.2.6 K_L identification

The CDC and the KLM are used.
K_L is neutral and longitudinal particle. So, it is difficult to detect. But K_L makes hadronic interaction at the ECL, solenoid and the KLM. Therefore, the condition of identification is similer to γ, existence of hitted cluster in the KLM and no matching with any charged tracks extrapolated from the CDC.

About main purpose of $B^0 \to J/\psi K_L$, kinematic fit which checks the direction correlation between reconstructed J/ψ and K_L is applied.

Bibliography

[1] J. H. Christensen *et al.*, Phys. Rev. Lett. **13**, 138 (1964).

[2] A. D. Sakharov, JETP Lett. 5, 24 (1967).

[3] S. Weinberg, Phys. Rev. Lett. **19**, 1624 (1967).

[4] M. Kobayashi and T. Maskawa, Prog. Theor. Phys. **49**, 652 (1973).

[5] A. Carter and A. I. Sanda, Phys. Rev. Lett. **45**, 952 (1980); Phys. Rev. **D23**, 1567 (1981); I. I. Bigi and A. I. Sanda, Nucl. Phys. **193**, 851 (1981).

[6] The BELLE Collaboration, "**Letter of intent for A study of CP violation in B meson Decays**", Apr., 1994.

[7] R. Fulton *et al.*, (CLEO), Phys. Rev. Lett. **64**, 16 (1990).

[8] H. Albrecht *et al.*, (ARGUS), Phys. Lett. **B234**, 409 (1990).

[9] M. Yamaga, Master thesis, Tohoku University, 1997.

[10] R. E. Kalman, Trans. ASME, J. Bas. Eng. **82D**, 35 (1960); R. E. Kalman and R. S. Bucy, Trans. ASME, J. Bas. Eng. **82D**, 95 (1961).

[11] R. Frühwirth, Nucr. Instr. and Meth.. **A262**, 444 (1987).

[12] I. Gavrilenko *et al.*, ATLAS Internal Note INDET-DRAFT, July, 1996.

[13] R. Luchsinger and C. Grab Comp. Phys. Comm. **76**, 263-280 (1993).

[14] T. Houjo, Master thesis, Osaka university, February 1999.

[15] GEANT Detector Description and Simulation Tool, CERN Program Library Long Writeup W0513.

[16] Y. Teramoto, "mu2, Muon Identification Program" :
`http://bsunsrv1.kek.jp/~klm/software/BASF_MUID/mu2_old/html/index.html`,
(1999).

[17] B. C. K. Casey, BELLE internal note 296, (2000).

[18] R. Balest *et al.*(CLEO), CLNS 94/1315, CLEO 94-26 December 14,
1994

[19] Review of Particle Physics, C. Caso *et al*, The European Physics Journal, **3**, 1 (1998).

[20] "KEKB B-Factory Design Report", KEK Report 95-7, (1995).

[21] DST production group, "Skimmed Files from Current DST Processing" :
`http://bsunsrv1.kek.jp/.secret/runinfo/dst/skimmed_file/SkimmedFile/`
`e000005/index_exp5.html`, (2000).